The Journal of Immunology

RESEARCH ARTICLE | APRIL 01 2018

PARP14 Controls the Nuclear Accumulation of a Subset of Type I IFN–Inducible Proteins

Greta Caprara; ... et. al

J Immunol (2018) 200 (7): 2439–2454.
https://doi.org/10.4049/jimmunol.1701117

PARP14 Controls the Nuclear Accumulation of a Subset of Type I IFN–Inducible Proteins

Greta Caprara,* Elena Prosperini,† Viviana Piccolo,† Gianluca Sigismondo,‡ Alessia Melacarne,* Alessandro Cuomo,* Mark Boothby,§ Maria Rescigno,*,¶ Tiziana Bonaldi,* and Gioacchino Natoli*,‖

The enzymes of the poly-ADP-ribose polymerase (PARP) superfamily control many relevant cellular processes, but a precise understanding of their activities in different physiological or disease contexts is largely incomplete. We found that transcription of several *Parp* genes was dynamically regulated upon murine macrophage activation by endotoxin. PARP14 was strongly induced by several inflammatory stimuli and translocated into the nucleus of stimulated cells. Quantitative mass spectrometry analysis showed that PARP14 bound to a group of IFN-stimulated gene (ISG)–encoded proteins, most with an unknown function, and it was required for their nuclear accumulation. Moreover, PARP14 depletion attenuated transcription of primary antiviral response genes regulated by the IFN regulatory transcription factor 3, including *Ifnb1*, thus reducing IFN-β production and activation of ISGs involved in the secondary antiviral response. In agreement with the above-mentioned data, PARP14 hindered *Salmonella typhimurium* proliferation in murine macrophages. Overall, these data hint at a role of PARP14 in the control of antimicrobial responses and specifically in nuclear activities of a subgroup of ISG-encoded proteins. *The Journal of Immunology*, 2018, 200: 2439–2454.

The enzymes of the poly-ADP-ribose polymerase (PARP) superfamily (1), also indicated as ADP-ribosyltransferase diphtheria toxin–like (ARTD) (2), are involved in a broad range of cellular activities, notably DNA repair and transcription (3), but the specific functions of most of them in different physiological or pathological conditions are still largely unknown.

Three PARP superfamily members, the macro-PARPs, possess one to three tandem macrodomains (2, 4, 5) and include two active mono-ADP-ribosyltransferases, PARP14 (ARTD8) and PARP15 (ARTD7, absent in the mouse), and an inactive enzyme, PARP9 (ARTD9) (2, 5–7). Murine PARP14, also called collaborator of STAT6, was described to associate with the transcription factor STAT6 and to coregulate IL-4–induced, STAT6-dependent gene expression in a manner that required its catalytic activity (8–10). Moreover, in murine macrophages, PARP14 was also shown to regulate, at a posttranscriptional level, the expression of tissue factor, a mediator of thrombosis and inflammation (11). PARP9 has also been shown to act as a transcriptional coactivator in B lymphocytes, where it is able to increase the expression of some IFN-stimulated genes (ISGs) (12); moreover, by binding to the E3 ligase deltex E3 ubiquitin ligase 3L (DTX3L), it acts as a STAT1-associated component of type I IFNR signal transduction, thus promoting ISG expression (13). Several PARP enzymes have been demonstrated to participate in inflammatory responses and host defense against infections. Specifically, PARP13 was shown to direct viral RNA degradation (14–17), whereas the IFN-inducible PARP12 exerts broad-spectrum antiviral activities (18, 19).

This study started from the observation that the expression of several PARPs was induced in mouse bone marrow–derived macrophages (BMDMs) by various inflammatory stimuli. We set out to mechanistically investigate one PARP protein, PARP14, whose expression and nuclear translocation were strongly induced by LPS stimulation. LPS signaling through TLR4 induces hundreds of genes, including primary response genes (PRGs) and, based on their requirement for new protein synthesis, secondary response genes (SRGs) (20), with *Ifnb1* and ISGs being representative of the first and the second group, respectively. We found that PARP14 coimmunoprecipitated with a selected group of ISG-encoded proteins, and that it enabled their nuclear accumulation. Additionally, PARP14 depletion reduced transcription of primary IFN regulatory

*Department of Experimental Oncology, European Institute of Oncology, 20139 Milan, Italy; †Humanitas Clinical and Research Center, 20089 Rozzano, Milan, Italy; ‡German Cancer Research Center, 69120 Heidelberg, Germany; §Vanderbilt University School of Medicine, Nashville, TN 37232; ¶Department of Biosciences, University of Milan, 20133 Milan, Italy; and ‖Humanitas University, 20089 Rozzano, Milan, Italy

ORCID: 0000-0003-3041-344X (A.M.).

Received for publication August 3, 2017. Accepted for publication January 29, 2018.

This work was supported by Italian Ministry of University and Research "Fondo per gli Investimenti della Ricerca di Base" Grant RBAP11H2R9. The funders had no role in study design, data collection and analysis, decision to publish, or preparation of the manuscript. Work in T.B.'s laboratory was supported by grants from the Italian Association for Cancer Research, the Italian Ministry of Health, and the National Research Council of Italy EPIGEN flagship project.

The raw data sets presented in this article have been submitted to the Gene Expression Omnibus database (https://www.ncbi.nlm.nih.gov/geo/query/acc.cgi) under accession number GSE100893.

Address correspondence and reprint requests to Dr. Greta Caprara or Dr. Gioacchino Natoli, European Institute of Oncology, Via Adamello 16, 20139 Milan, Italy (G.C.) or Humanitas University, School of Medicine, Via Manzoni 113, 20089 Rozzano, Milan, Italy (G.N.). E-mail addresses: greta.caprara@ieo.it (G.C.) or gioacchino.natoli@hunimed.eu (G.N.)

The online version of this article contains supplemental material.

Abbreviations used in this article: ACN, acetonitrile; ARTD, ADP-ribosyltransferase diphtheria toxin–like; BMDM, bone marrow–derived macrophage; ChIP, chromatin immunoprecipitation; ChIP-seq, ChIP sequencing; DTX3L, deltex E3 ubiquitin ligase 3L; FDR, false discovery rate; H3K27ac, histone H3 lysine 27 acetylation; IFI35, IFN-induced protein 35; IRF, IFN regulatory transcription factor; ISG, IFN-stimulated gene; KO, knockout; LC-MS/MS, liquid chromatography–tandem MS; MS, mass spectrometry; Nmi, N-myc and STAT interactor; PARP, poly-ADP-ribose polymerase; Pol II, polymerase II; PRG, primary response gene; qCML, quantile-adjusted conditional maximum likelihood; RNA-seq, RNA sequencing; RPKM, reads per kilobase of transcript per million mapped reads; RT-qPCR, quantitative RT-PCR; shRNA, short hairpin RNA; SILAC, stable isotope labeling with amino acids in cell culture; SQSTM1, sequestosome 1; SRG, secondary response gene; 4sU, 4-thiouridine; UCSC, University of California Santa Cruz; WT, wild-type.

transcription factor (IRF)3–regulated genes, including *Ifnb1*, and, as a consequence, of secondary IFN-β–stimulated genes. Consistently, PARP14 hampered *Salmonella typhimurium* proliferation in macrophages. Overall, these data indicate that PARP14 is an additional and nonredundant component of the IFN response.

Materials and Methods

Abs and reagents

Affinity-purified rabbit polyclonal Abs against mouse PARP14 were generated in-house using recombinant proteins corresponding to PARP14 aa 81–270 (NP_001034619.2). Affinity-purified rabbit polyclonal Abs against mouse PARP12 were generated in-house using recombinant proteins corresponding to PARP12 aa 507–690 (NP_766481.2). Affinity-purified rabbit polyclonal Abs against mouse DTX3L and PARP9 were generated in-house using recombinant proteins corresponding to DTX3L aa 61–240 (NP_001013389.2) and PARP9 aa 623–831 (NP_084529.1). Affinity-purified rabbit polyclonal Abs against mouse N-myc and STAT interactor (NMI) and IFN-induced protein 35 (IFI35) were generated in-house using recombinant proteins corresponding to NMI aa 1–123 (NP_001135421.1) and IFI35 aa 1–33 (NP_081596.1). The other Abs used were: anti-p62 mouse monoclonal (Novus Biologicals), anti-vinculin (Sigma-Aldrich), anti-tubulin (Sigma-Aldrich), anti–lamin B1 (Abcam), anti-STAT1 (no. 9172; Cell Signaling Technology), anti– phospho-STAT1 (no. 7649; Cell Signaling Technology), anti-IRF3 (no. 4302; Cell Signaling Technology), and anti–phospho-IRF3 (no. 4947; Cell Signaling Technology). LPS from *Escherichia coli* serotype 055:B5 (Sigma-Aldrich) was used at 100 ng/ml, IFN-γ (R&D Systems) was used at 10 IU/ml, IFN-β (Millipore) was used at 100 IU/ml, Pam3CSK4 (InvivoGen) was used at 0.5 μg/ml, polyinosinic-polycytidylic acid (InvivoGen) was used at 10 μg/ml, ODN1826 (InvivoGen) was used at 5 μM, and JAK inhibitor I (CAS 457081-03-7; Calbiochem) was used at 100 nM.

Western blots

Cells were lysed either in cytosolic extraction buffer (50 mM Tris HCl [pH 8], 60 mM KCl, 0.1% Nonidet P-40, 2 mM EDTA, 10% glycerol) or E1A buffer (for nuclear and total extraction) (50 mM HEPES, 250 mM NaCl, 0.5% Nonidet P-40, 1 mM EDTA) containing protease inhibitors, 1 mM PMSF and 1 mM NaF. Ten to thirty micrograms of clarified cell extracts was resolved on SDS–polyacrylamide gels and blotted onto nitrocellulose membranes (Schleicher & Schuell). After blocking, filters were incubated with the specific Ab. The bound secondary Ab was revealed using the ECL method (Amersham Biosciences).

Immunoprecipitation

Primary Abs were added to the nuclear lysates and incubated with rotation overnight at 4°C. Thirty microliters of a 50% slurry of protein A–Sepharose (Amersham Biosciences) was then added and the incubation was continued for an additional 1 h. Immunoprecipitates were extensively washed with E1A buffer. Immunoprecipitated proteins were resolved by 10 or 12% SDS-PAGE, and then transferred to nitrocellulose ECL membranes (Schleicher & Schuell). After blocking, filters were incubated with the specific Ab. The bound secondary Ab was revealed using the ECL method (Amersham Biosciences).

Cell culture

Bone marrow cells isolated from female Fvb/Hsd mice were differentiated in macrophages as described (21). Stimulations were carried out at day 7 after plating. The RAW 264.7 mouse macrophage cell line was purchased from the American Type Culture Collection. Cells were grown in DMEM containing 10% FBS and 2 mM glutamine. PARP14 wild-type (WT) and null bone marrow cells (22) were a gift of M. Boothby.

Lentiviral infection

RAW 264.7 macrophages were exposed (twice) to the supernatant of packaging ecotropic Phoenix cells transiently transfected with the specific lentiviral vectors (lentiCRISPR v2 empty or lentiCRISPR v2 containing the single-guide sequence specific to NMI).

Transfections

RAW 264.7 macrophages (10×10^6 cells) were transfected by electroporation using 10 μg of the DNA of interest. Electroporation was performed with a MicroPorator (Digital Bio Technology) at the following conditions: 1680 V, 20 ms, one pulse. Electroporated cells were then plated in 10 ml of medium on 10-cm dishes at 37°C in a 5% CO_2 atmosphere.

Short hairpin RNA plasmid

PARP14 short hairpin RNA (shRNA) constructs were based on the pLMP retroviral vector (23) using the following oligonucleotides: sh1, 5′-GAATTAGCAGAGACGTGAT-3′; sh2, 5′-CGGAATTAGCAGAGACGTGATA-3′. To generate stably transfected clones, 2 d after electroporation, cells were split and selected with 3 μg/ml puromycin for 2 wk. Stable expressing clones were then plated by limiting dilution and expanded.

CRISPR/Cas9 genome editing

Single-guide sequences specific to PARP14 (exon 1) and NMI (exon 1) were constructed using the CRISPR design tool (http://tools.genome-engineering.org) (24) and cloned into pSpCas9(BB)-2A-GFP [described in Ran et al. (24) and provided by Addgene (plasmid no. 48138)] and lentiCRISPR v2 [described in Sanjana et al. (25); plasmid no. 52961 (Addgene) was a gift from F. Zhang], respectively. The sequences selected, based on the lowest number of predicted off-targets in exons and the highest predicted efficiency, were as follows: PARP14, 5′-CACCGTGCGAGGTCGTCCCGGAGC-3′; NMI. 5′-CACCGCAGAGATGGACGATATGAG-3′.

After electroporation, single cells were seeded in 96-well plates by dilution and expanded. Clones were screened by Western blot and their genomic DNA was sequenced, confirming the mutations.

Quantitative RT-PCR

RNA was extracted from macrophages using a Quick-RNA MiniPrep (Plus) kit (Zymo Research), and cDNA was prepared from 1 μg of total RNA with an ImProm-II reverse transcription system (Promega) following the manufacturers' instructions. Quantitative RT-PCR (RT-qPCR) was assembled with Fast SYBR Green master mix and run on a 7500HT ABI Prism machine (Applied Biosystems). Analysis (SDS v2.0.6 software; Applied Biosystems) was achieved following minimum information for publication of RT-qPCR experiments guidelines, and primer design was performed using the Roche Universal Probe Library Assay Design Center (https://lifescience.roche.com/en_it/brands/universal-probe-library.html). The primers used for RT-qPCR are listed in Table I.

4-Thiouridine labeling

For 4-thiouridine (4sU) experiments, RAW 264.7 cells were labeled with 4sU (150 μM; Sigma-Aldrich) for 10 min and the labeled RNA was isolated as described (26). A total of 160 ng of 4sU-labeled RNA was used for cDNA retrotranscription. The primers used to detect 4sU labeled cDNA are listed in Table II.

Chromatin immunoprecipitation

Chromatin immunoprecipitation (ChIP) assays were carried out as previously described (21). After chromatin shearing by sonication, lysates were incubated overnight at 4°C with protein G Dynabeads (Invitrogen) coupled with 10 μg of anti-IRF8 (rabbit polyclonal Ab raised in-house and affinity purified), PU.1 (rabbit polyclonal Ab generated in-house against the N terminus of PU.1 [aa 1–100]; NP_035485.1) and RNA polymerase II (Pol II) Abs (sc-899; Santa Cruz Biotechnology) or 10 μg of rabbit IgG (sc-2027; Santa Cruz Biotechnology). The primers used to detect chromatin-immunoprecipitated genomic DNA are listed in Table III.

Infection of RAW 264.7 macrophages with S. typhimurium

RAW 264.7 cells (4×10^5) were seeded in 24-well plates the day before infection. A WT invasive strain of *S. typhimurium* in the SL1344 background was used to infect RAW 264.7 macrophages. Single bacterial colonies were grown overnight and restarted the next day, at 1:10 of the original volume, to reach an absorbance at 260 nm of 0.6, corresponding to 0.6×10^9 CFU/ml. Macrophages were infected with a cell-to-bacteria ratio of 1:10 in antibiotic-free DMEM for 90 min at 37°C. Cells were then washed and medium was replaced with DMEM containing 50 μg/ml gentamicin.

NO production assay (Griess assay)

Supernatants from *S. typhimurium*–infected and untreated RAW 264.7 macrophages were collected after 24 h from infection, and accumulation of nitrite (the oxidized product of NO) was evaluated as previously described (27). All chemicals were obtained from Sigma-Aldrich. Aliquots

of 100 μl of cell culture supernatant were mixed with equal volumes of Griess reagent (1% sulfanilamide, 0.1% naphthylenediamine dihydrochloride, 2.5% H_3PO_4) at 37°C for 15 min. Sodium nitrite was used to generate a standard curve for NO production, and peak absorbance was measured at 560 nm with a GloMax explorer system (Promega). Cell-free medium alone, used to blank absorbance readings, contained <0.5 μM NO_2^- per well.

Determination of bacterial counts

Seven hours after *S. typhimurium* infection, RAW 264.7 macrophages were detached, counted, lysed with 0.5% sodium deoxycholate, and plated in quadruplicate on agar plates to evaluate bacterial content. After overnight culture, bacterial colonies were counted.

Statistical analysis

A Student *t* test, parametric one-way or two-way ANOVA (with a Tukey or Sidak posttest, respectively), Wilcoxon rank sum test, and Wilcoxon signed rank test were used as indicated. Analyses were done using GraphPad Prism 6.

ChIP sequencing and RNA sequencing

ChIP sequencing (ChIP-seq) and RNA sequencing (RNA-seq) were carried out using previously described protocols (28) on an Illumina HiSeq 2000 platform. Two to 5×10^6 (histone marks) or 20–40 $\times 10^6$ (transcription factors) fixed cells were lysed to prepare nuclear extracts. After chromatin shearing by sonication, lysates were incubated overnight at 4°C with protein G Dynabeads (Invitrogen) coupled with 5 μg of anti-histone H3 (acetyl K27) Ab (ab4729; Abcam) or 5 μg of rabbit IgG (sc-2027; Santa Cruz Biotechnology). After immunoprecipitation, beads were recovered using a magnet and washed; chromatin was eluted and cross-links were reverted overnight at 65°C. DNA was either purified with QiaQuick columns (Qiagen) or solid-phase reversible immobilization beads (Agencourt AMPure XP; Beckman Coulter) and quantified with PicoGreen (Invitrogen). DNA libraries were prepared for HiSeq 2000 sequencing as previously described (29).

Total RNA was extracted from 1–4 $\times 10^6$ cells using Maxwell 16 LEV Simply RNA cells kit (Promega) and run on an Agilent Bioanalyzer 2100 to asses sample integrity. mRNA sequencing library preparation from 1 μg of total RNA (RNA integrity of >9) was performed with a TruSeq RNA sample preparation kit (Illumina) according to the manufacturer's instructions.

Computational methods

Single-end reads (51 nt) were quality filtered according to the Illumina pipeline and mapped to the mm10 reference genome. For ChIP-seq, reads were mapped using bowtie2 v2.2.6 (30). Default parameters were used with the options –very-sensitive,–no-unal and with the prebuilt bowtie2 index. Only uniquely mapping reads were retained. Peak calling for acetylation was performed with SICER v1.1 (31) using a redundancy threshold of 1, a window size of 200 bp, a gap size of 600 bp, and a false discovery rate (FDR) cutoff of 1×10^{-3}. Fragment size was set to 150 and the effective genome fraction to 0.80. RNA-seq reads were mapped using TopHat v2.1.0 with the option –b2-very-sensitive (32). Differential expression was evaluated with an exact test for the negative binomially distributed counts using edgeR v3.10.5 with the limma v3.24.15 Bioconductor package (33–35).

Detailed ChIP-seq analysis

After quality filtering, according to the Illumina pipeline, histone H3 lysine 27 acetylation (H3K27ac) short reads (51 bp) were mapped with bowtie2 v2.2.6 (30) to the mm10 reference genome downloaded from Illumina's iGenome archive (University of California Santa Cruz [UCSC] collection, http://support.illumina.com/sequencing/sequencing_software/igenome.html). We used default parameters with the options –very-sensitive,–no-unal and with the prebuilt bowtie2 index. Only uniquely mapping reads were retained. Peak calling was performed using SICER v1.1 (31, 36, 37). We identified significantly enriched clusters using a redundancy threshold of 1, a window size of 200 bp, a gap size of 600 bp, and a FDR cutoff of 0.01. Fragment size was set to 150 and the effective genome fraction was set to 0.80. Each ChIP was compared with genomic DNA derived from RAW 264.7 macrophages. Regions that overlap with the blacklists identified by the ENCODE and modENCODE consortia (38) were filtered out. The mm9 blacklist file was downloaded (http://www.broadinstitute.org/~anshul/projects/mouse/blacklist/mm9-blacklist.bed.gz) and converted into the mm10 genome assembly with the tool liftOver developed by the UCSC Genome Browser (39) using default parameters.

Genome-wide analysis of H3K27 acetylation distribution. We selected 5500 induced regions in which the H3K27 acetylation signal, at 2 h after LPS stimulus, was statistically enriched with respect to both the input DNA, derived from RAW 264.7 macrophages, and to the untreated condition (intensity of signal > 2-fold, FDR ≤ 0.01). For each condition and at each time point, we adjusted counts to reads per kilobase per million mapped reads. To evaluate how H3K27 acetylated regions respond to endotoxin treatment, the $\log_2$ ratio (R) of the normalized reads counts in LPS-stimulated PARP14 knockout (KO) versus wild-type (WT) cells were calculated. All blocks were divided into three groups according to the R value. We classified 4520 regions not affected by PARP14 KO ($-1 < R > +1$), 129 regions that increased after PARP14 KO ($R \geq 1$), and 851 regions that decreased after PARP14 depletion ($R \leq -1$). A golden set of PARP14-independent regions ($n = 942$) according to the ratio R ($-0.15 < R < 0.15$) was selected. The plot and the box plots were generated using the $\log_2$-transformed intensity of signal.

Motif enrichment analysis. To identify overrepresented motifs corresponding to known transcription factor binding sites, Pscan (40) was run on the acetylated regions. We focused on 500 bp surrounding the nucleotide located in the middle point of the SICER block. All of the LPS-induced acetylated blocks presenting a reduction upon PARP14 depletion ($n = 851$) were scanned against the general background from the FANTOM5 database for mm9 (41, 42) after conversion into the mm10 genome assembly, using the liftOver tool of the UCSC Genome Browser (39). Acetylated regions were scanned with 3041 models (position weight matrices) collected from the literature (JASPAR 2014, http://jaspar.binf.ku.dk/; JASPAR 2016, http://jaspar.genereg.net/; HOCOMOCO v10, http://www.cbrc.kaust.edu.sa/hocomoco10/human/mono) (7, 32, 43–49). In addition to that, the set of 851 acetylated regions was scanned against the regions not affected by PARP14 KO ($n = 942$).

Genomic regions enrichment annotation. To associate the isolated genomic peaks to a genetic function, we applied GREAT v3.0.0 (50) with the Molecular Signature Database pathway.

Detailed RNA-seq analysis

After quality filtering, according to the Illumina pipeline, 51 nt single-end reads (RAW 264.7 macrophages and primary BMDMs) were mapped to the mm10 reference genome and to the *Mus musculus* transcriptome (Illumina's iGenomes reference annotation downloaded from UCSC, http://support.illumina.com/sequencing/sequencing_software/igenome.html). TopHat v2.1.0 (32) was used with the option –very-sensitive. Indels due to sequencing errors will be discovered by bowtie2 v2.2.6 (30) using the option *–b2*. Differential expression analysis was evaluated with an exact test for the negative binomially distributed counts using edgeR v3.10.5 with limma v3.24.15 (Bioconductor package, https://bioconductor.org/packages/release/bioc/html/edgeR.html) (33–35). Read counts for edgeR analysis were obtained with the software HTSeq v0.6.1p1 (51) with the option –s no. To reduce the amount of bias in the experiments, we adjusted the standard cpm with the trimmed mean of M values using the *calcNormFactors()* function from the edgeR Bioconductor package. With respect to standard normalization, trimmed mean of M values normalization has the advantage to deeply reduce the false-positive rate (33). We modeled the data variability by estimating the dispersion of the negative binomial model using the quantile-adjusted conditional maximum likelihood (qCML) method. Initially we used the qCML *estimateCommonDisp()* function and then the qCML *estimateTagwiseDisp()* function, both from the edgeR Bioconductor package. We finally computed exact p values for the negative binomial distribution using the function *exactTest()*, making pairwise comparisons between the different groups.

PARP gene expression in LPS-treated BMDMs. Samples derived from the GSE88700 subseries (GSM2344465, GSM2344466, GSM2344467, and GSM2344468) (52) were analyzed: genes belonging to the PARP family were selected and the intensity of their expression ($\log_2$-transformed reads per kilobase of transcript per million mapped reads [RPKM]) was hierarchically clustered, using the complete-linkage method as algorithm and the Pearson correlation as distance metric. Statistically induced genes (FDR ≤ 0.05, according to the Benjamini–Hochberg correction and 2-fold) are indicated in red.

Effects of PARP14 depletion in the transcriptional response to LPS in RAW 264.7 macrophages. To detect the PARP14 KO-affected genes, we compared the LPS-treated WT versus the PARP14 KO replicates. The JAK-dependent gene labeling was obtained comparing the replicates stimulated with LPS against the LPS plus JAK inhibitor–treated ones. In both cases only genes with a FDR ≤ 0.01 and with a signal intensity of at least 2-fold were considered significant. To compare the expression between genes and to compensate for different gene lengths, we considered

also the RPKM (RPKM $\geq$ 1 in both replicates, in WT, after stimulation). Finally, we selected only coding genes according to the Mus_musculus. GRCm38.83.chr gtf file downloaded from Ensembl (http://ftp.ensembl.org/pub/release-83/gtf/mus_musculus/). The lists of known PRGs and SRGs were collected from the literature (53). PRGs were grouped based on their transcriptional regulation: IRF3-dependent and NF-κB/IRF3–dependent genes. The genes affected by PARP14 depletion, upon endotoxin treatment, were compared with the selected lists of PRGs and SRGs and finally clustered, according to their expression level (RPKM $\log_2$ transformed), using the complete-linkage method as algorithm and the Pearson correlation as distance metric.

Data availability

Raw data sets are available for download at the Gene Expression Omnibus database (https://www.ncbi.nlm.nih.gov/geo/query/acc.cgi) under accession number GSE100893. The secure token for data access is yrujwcsyhtsvpil.

Track visualization

All tracks were linearly rescaled to 1 million and visualized with the Integrative Genomics Viewer (54, 55).

Figures

All graphical representations were obtained with R packages (https://cran.r- project.org/).

Transcription factors binding sites detection

FIMO software (56), from the MEME Suite software toolkit (parameters –*parse-genomic-coord* and –*bgfile)* (57), was employed to detect specific transcription factors binding sites on the *Parp14* locus. The locus is positioned on the reverse strand with respect to the reference genome, and thus we extended −500/+250 bp around the *Parp14* transcription start site and we selected only matrixes mapping on the same strand.

Stable isotope labeling with amino acids in cell culture

For metabolic labeling, RAW 264.7 cells were grown in "heavy" and "light" stable isotope labeling with amino acids in cell culture (SILAC) media, prepared by adding to the SILAC DMEM, depleted of lysine and arginine (catalog no. FA30E15086; M-Medical, Pasching, Austria), the following ingredients: 10% dialyzed FBS (catalog no. 26400–044; Invitrogen), 1% glutamine, 1% penicillin/streptomycin, 10 mM HEPES (pH 7.5), and either the light isotope–encoded amino acids $^{12}C_6$ $^{14}N_2$ L-lysine (Lys^0, catalog no. L8662; Sigma-Aldrich) and $^{12}C_6$ $^{14}N_4$ L-arginine (Arg^0, catalog no. A6969; Sigma-Aldrich) or their heavy isotope counterparts, $^{13}C_6$ $^{15}N_2$ L-lysine (Lys^8, catalog no. 68041; Sigma-Aldrich) and $^{13}C_6$ $^{15}N_4$ L-arginine (Arg^{10}, catalog no. 608033; Sigma-Aldrich). Lysine and arginine were added at concentrations of 73 and 42 mg/l, respectively. RAW 264.7 cells were cultivated in SILAC media for up to nine generations, with careful monitoring of their growth rate, viability, and overall morphology, to ensure that normal physiology was preserved.

In-gel digestion of immunopurified proteins

Immunopurified samples were separated by one-dimensional SDS-PAGE using 4–12% NuPAGE Novex Bis-Tris gels (Invitrogen) and NuPAGE MES SDS running buffer (Invitrogen), according to the manufacturer's instructions. The gel was stained with Coomassie blue using a colloidal blue staining kit (Invitrogen). Processing of gel-separated proteins prior to mass spectrometry (MS) analysis was carried out as previously described (58), with minor modifications. Briefly, slices were cut from gel and destained in 50% (v/v) acetonitrile (ACN)/50 mM NH_4HCO_3. Reduction was carried out with 10 mM DTT in 50 mM NH_4HCO_3, followed by alkylation with 55 mM iodoacetamide in 50 mM NH_4HCO_3. In-gel digestion was performed with 12.5 ng/μl trypsin (V5113; Promega) in 50 mM NH_4HCO_3, overnight at 37˚C. Digested peptide were extracted with 3% trifluoroacetic acid, 30% ACN, and finally with 100% ACN, lyophilized, desalted, and concentrated on C18 stage tips (59). Peptides were eluted with high organic solvent (80% ACN), lyophilized, resuspended in 0.1% trifluoroacetic acid and 0.5% acetic acid in double distilled H_2O, and subjected to liquid chromatography–tandem MS (LC-MS/MS) analysis.

LC-MS/MS

Digested peptide were separated by nano–liquid chromatography using an Agilent 1100 series (Agilent Technologies, Waldbronn, Germany), coupled to a 7-Tesla linear ion trap–Fourier transform–ion cyclotron resonance ultra mass spectrometer (Thermo Fisher Scientific, Bremen, Germany). The nano-flow liquid chromatography system was operated in a one-column setup with a 15-cm analytical column (75 μm inner diameter, 350 μm outer diameter) packed with C_{18} resin (ReproSil-Pur C18-AQ, 3 mm; Dr. Maisch, Ammerbuch, Germany). Solvent A was 0.1% formic acid and 5% ACN in double distilled H_2O, and solvent B was 95% ACN with 0.1% formic acid. The sample was injected into an aqueous solution at a flow rate of 500 nl/min. Peptides were separated with a gradient of 0–36% during 120 min followed by gradients of 36–60% for 10 min and 60–80% over 5 min at a flow rate of 250 nl/min. No sheath, sweep, or auxiliary gasses were used, and the capillary temperature was set at 190˚C. The mass spectrometer was operated in data-dependent mode to automatically switch between MS and MS/MS acquisition. In the mass spectrometer, full scan MS spectra (200–1650 m/z) were acquired with a resolution of 10^5 at 400 m/z, setting an acquisition gain control target of 10^6. The five most intense ions were isolated for fragmentation in the linear ion trap using collision-induced dissociation at a target value of 5000. Singly charged precursor ions were excluded. In the MS/MS method, a dynamic exclusion of 30 s was applied, and the total cycle time was ∼2 s. The collision gas pressure was 1.3 millitorr, and the normalized collision energy using wide band activation mode was 35%. The ion selection threshold was 250 counts with an activation q of 0.25. An activation time of 30 ms was applied in MS/MS acquisitions.

Data analysis and peptide assignment by MaxQuant

Mass spectrometric raw data were analyzed with MaxQuant software, v1.3.0.5. Filtered MS/MS spectra were searched by Andromeda search engine (60) against the UniProt sequence database (Mouse1301 containing 33,202 entries). Enzyme specificity was set to trypsin, allowing cleavage N-terminal to proline. Peptide identification was based on a search with mass deviation of the precursor ion of 7 ppm and the fragment mass tolerance was set to 0.5 Da. An FDR of 0.01 for proteins and peptides and a minimum peptide length of 6 aa were required. Carbamidomethylation of cysteine was selected as a fixed modification, whereas acetylation on protein N-terminal and methionine oxidation were set as variable modifications in the Andromeda search. The modifications corresponding to arginine and lysine labeled with heavy stable isotopes ($^{13}C_6$ $^{15}N_4$ L-arginine and $^{13}C_6$ $^{15}N_2$ L-lysine, Arg^{10} and Lys^8, respectively) were treated as fixed modifications in the Andromeda

Table I. RT-qPCR primer sequences

	Sense Primer	Antisense Primer
Tbp	5′-CTGGAATTGTACCGCAGCTT-3′	5′-TCCTGTGCACACCATTTTTC-3′
Parp14	5′-TGGAGATCCTAGTGACAAAAATCC-3′	5′-CTGGAAAGGCTCCCATAGATAC-3′
Ifnb1	5′-CACAGCCCTCTCCATCAACTA-3′	5′-CATTTCCGAATGTTCGTCCT-3′
Ccl5	5′-ACCATATGGCTCGGACACCACT-3′	5′-ACTGCAGACTGGCTGAAAGC-3′
Cxcl10	5′-CGCTGCAACTGCATCCATATCG-3′	5′-CCGGATTCAGACATCTCTGCTC-3′
Isg15	5′-AGTCGACCCAGTCTCTGACTCT-3′	5′-CCCCAGCATCTTCACCTTTA-3′
Ifit1	5′-GCTCTGCTGAAAACCCAGAG-3′	5′-CCCAATGGGTTCTTGATGTC-3′
Nfkbia	5′-CTTGGCTGTGATCACCAACCAG-3′	5′-CGAAACCAGGTCAGGATTCTGC-3′
Cmpk2	5′-GAACCTCATCTGCACCCATT-3′	5′-GTGGCATCCAGTCCTTCAAT-3′
Rsad2	5′-TCTGGAGGAGAACCCTTCCT-3′	5′-AACCTGCTCATCGAAGCTGT-3′
Mx2	5′-ACACTCTGTCTCCAAGCCG-3′	5′-ACAAACTGTCACTGTCCCCA-3′

Table II. 4sU-labeled cDNA primer sequences

	Sense Primer	Antisense Primer
Ccl5	5′-AGAAGGGGAGGTCTGGGTAT-3′	5′-TCACCATCATCCTCACTGCA-3′
Cxcl10	5′-AATGGCCTTGGTGTCCCTTA-3′	5′-AGAGACATCCCGAGCCAAC-3′
Isg15	5′-ACGGACACCAGGAAATCGTT-3′	5′-GGGTCACTACAACTCCAGGA-3′
Ifit1	5′-ACCCAGAGAACAGCTACCAC-3′	5′-ATCCTTGTTCCCCATCAGCA-3′
Nfkbia	5′-TCCCTTCACCTGACCAATGA-3′	5′-GGTTTCCCTGTCATCCCTCA-3′

search. Additional peptides identified by enabling the "match between run" option in MaxQuant, setting the retention time window (after realignment of the runs) to 2 min based on the accurate mass measurement output from MaxQuant, were manually filtered as follows: protein identified were accepted only when they contained two peptides, at least one of which was unique (peptide > 1, unique > 0). Proteins quantified were considered for further analysis only when they had a ratio count (RC) > 1 (Supplemental Table II). Protein normalized ratios were $\log_2$ transformed and plotted as histogram by Perseus software (61). The calculated histogram fits with a bimodal distribution, and upregulated proteins were selected within the top 10% of total protein ratio distributions.

Results

Induction of PARP14 by inflammatory stimuli

Transcription of several PARP superfamily genes was dynamically regulated upon LPS treatment of mouse BMDMs (Fig. 1A). Among them, *Parp14* mRNA was detected at negligible levels in unstimulated cells and then strongly upregulated. The gene encoding *Parp14* is located on chromosome 16qB3, and based on an *in silico* analysis (FIMO software) it was found to contain STAT1, IRF1, and NF-κB DNA binding motifs in the genomic regions corresponding to the 5′ untranslated region and the first intron of the gene (Supplemental Table I). *Parp14* mRNA was also rapidly upregulated both in BMDMs and in the RAW 264.7 macrophage cell line upon treatment with IFN-γ plus LPS (Fig. 1B) and with IFN-β administered alone (Fig. 1C). Other TLR agonists, namely polyinosinic-polycytidylic acid (TLR3), unmethylated CpG-containing DNA sequences (ODN1826, TLR9 agonist), and Pam3CSK4 (TLR1/2) also stimulated *Parp14* expression to a various extent (Fig. 1D).

We raised a polyclonal Ab that efficiently and specifically recognized the endogenous protein. Consistent with the mRNA data, the PARP14 protein was expressed at low basal levels and upregulated after LPS stimulation (Fig. 1E, upper panel). Moreover, although it was mainly localized in the cytosolic compartment in unstimulated cells, it was also readily detectable in the nucleus after LPS stimulation (Fig. 1E, lower panel).

PARP14 interacts with ISG-encoded proteins and enables their nuclear accumulation

The presence of PARP14 in the nucleus of LPS-stimulated macrophages hinted at its possible role in mediating some nuclear effects elicited by LPS, a possibility also suggested by previous reports describing a transcriptional coregulator activity of PARP14 (8–10). To gain insight into the possible functions of PARP14 in the nucleus, we used a quantitative SILAC-based MS approach to identify PARP14 interactors in endotoxin-stimulated mouse macrophages. Briefly, RAW 264.7 clones stably harboring an shRNA specific for PARP14 (shRNA no. 1, Fig. 2A) and their WT counterpart (harboring a scrambled control shRNA) were grown in light and heavy SILAC medium, respectively. After LPS treatment, cells were harvested, the nuclear proteins were extracted, and PARP14 immunoprecipitates from the two cell populations were then mixed in equal amounts (1:1), in-gel digested, and subjected to quantitative high-resolution MS analysis (Fig. 2B). Proteins were quantified and SILAC protein ratios calculated through the MaxQuant algorithm (62). Putative PARP14 interactors, coenriched with the bait in the heavy SILAC channel, were identified within the top 10% of total protein SILAC ratio distributions, indicated in red in Table IV. We found that many PARP14 binders were encoded by IFN-stimulated genes (Table IV, Supplemental Table II). We validated the binding with these interactors by standard coimmunoprecipitation followed by Western blot analysis in LPS-treated RAW 264.7 macrophages (Fig. 2C). The E3 ligase DTX3L and the macro-PARP PARP9, whose genes share a common IFN-γ–responsive bidirectional promoter (12) and form a stable dimeric complex (13, 63), were clearly detected in PARP14 immunoprecipitates. Moreover, the IFN-inducible PARP12, which was shown to possess antiviral activity (18, 19), also efficiently interacted with PARP14. Interestingly, we also validated as PARP14 interactors the sequestosome 1 (SQSTM1)/p62, a multifunctional scaffold protein involved in autophagy, signal transduction, cell death, and inflammation (64–66). Finally, we validated PARP14 binding to two ISG products, namely NMI and IFI35 (67, 68), which associate into a stable high–molecular mass complex (69, 70). NMI was reported to bind STAT family transcription factors and to potentiate STAT1- and STAT5-dependent transcription (71), whereas IFI35 was shown to be involved in the control of AP-1–mediated gene transcription (72). In line with the interaction data, PARP14 and its binding partners were similarly detected in the nuclear fraction after LPS stimulation (Fig. 2D).

Table III. ChIP qPCR primer sequences

	Sense Primer	Antisense Primer
Ifnb1 Irf8-PU.1 binding	5′-GATGGTCCTTTCTGCCTCAG-3′	5′-TCCAGCAATTGGTGAAACTG-3′
Ifnb1 Pol II binding	5′-GAGAAGCACAGCAGGAACG-3′	5′-AGGGAGAACTGAAAGTGGGA-3′
Ccl5	5′-GGCCCTACTGACAAGGTGAC-3′	5′-GAGCTGTCCTGTGTGGTGAA-3′
Cxcl10	5′-ACTCTGCAAGCTGAAGGGAT-3′	5′-GCCGTCATTTTCTGCCTCAT-3′
Isg15	5′-TGAAACCCATCTGCCTCTGT-3′	5′-TCTTCACACCCACAGCTCAT-3′
Ifit1	5′-CAAGGCAGGTTTCTGAGGAG-3′	5′-TAGCATCCTTGTTCCCCATC-3′
Nfkbia	5′-AGAGGGCTGGGGTTACTGAG-3′	5′-CTAGAAAAAGAACTGGCTCGTCC-3′

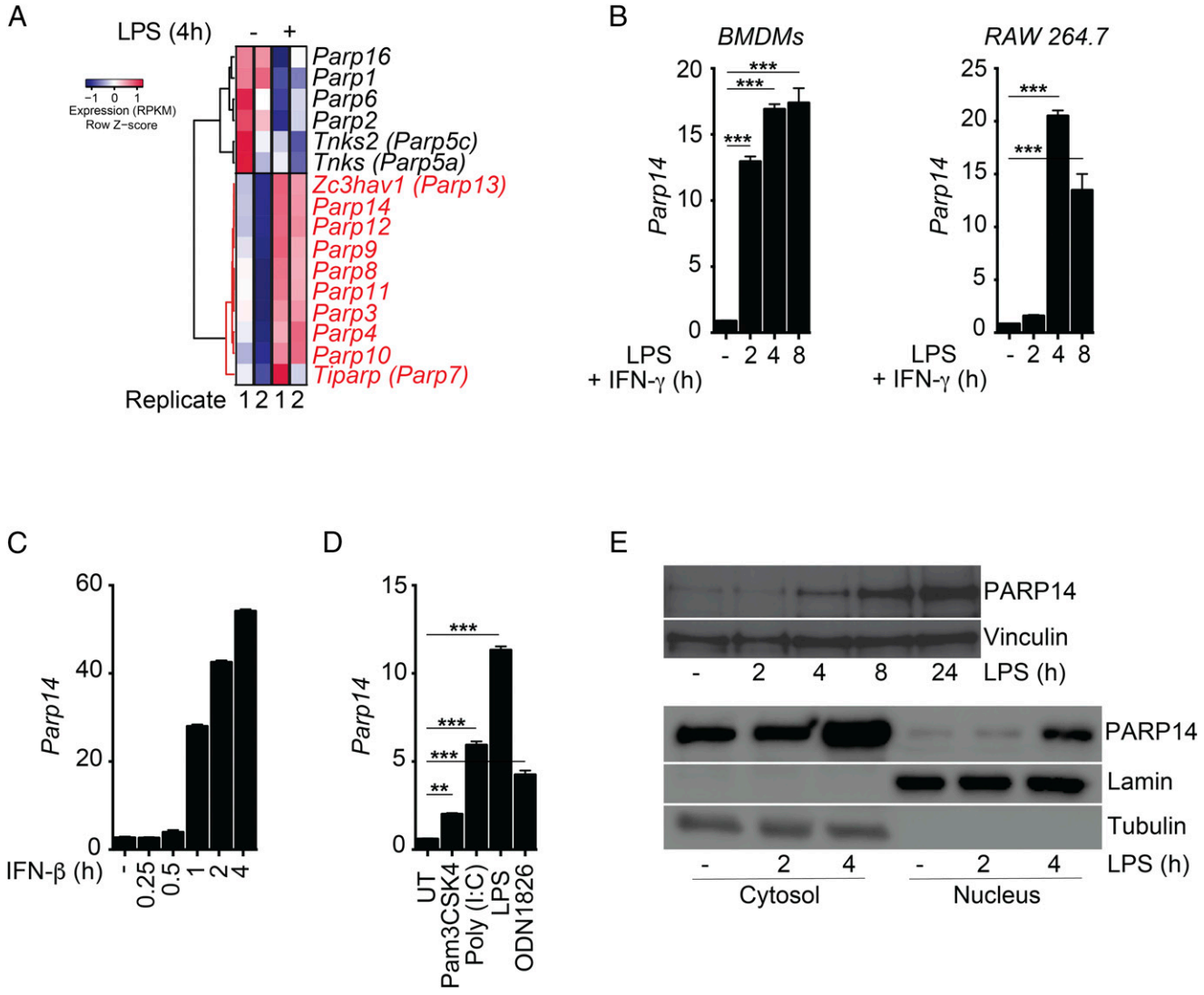

FIGURE 1. Induction of PARP14 by inflammatory stimuli in mouse macrophages. (**A**) Heat map, generated from the datasets published in Curina et al. (52), showing *Parp* genes differential expression, in primary BMDMs, upon LPS treatment. The color bar indicates the intensity of gene expression (red indicates highly expressed genes; blue indicates lowly expressed genes). *Parp* genes were hierarchically clustered using the complete-linkage method as algorithm and the Pearson correlation as distance metric: two major clusters are shown. Statistically significant induced genes are depicted in red (FDR $\leq$ 0.05, 2-fold, RPKM $\geq$1). (**B**) Kinetics of *Parp14* mRNA upregulation in primary BMDMs (left) and RAW 264.7 macrophage cell lines (right) upon LPS and IFN-γ stimulation. Data are displayed as ratio to the *TBP* mRNA. Data represent the mean of three independent experiments each performed in triplicate ($n = 3$). Significance was determined by one-way ANOVA with a Tukey posttest. ***$p < 0.001$. (**C**) Kinetics of *Parp14* mRNA upregulation in primary BMDMs after IFN-β stimulation. Data are displayed as ratio to the *TBP* mRNA. Data are from one experiment, performed in triplicate ($n = 3$), representative of three independent ones. The error bars indicate the SEM. (**D**) Effect of TLR agonists treatment on *Parp14* mRNA levels in primary BMDMs. Data are displayed as ratio to the *TBP* mRNA. Data represent the mean of three independent experiments each performed in triplicate ($n = 3$). Significance was determined by one-way ANOVA with a Tukey posttest. **$p < 0.01$, ***$p < 0.001$. (**E**) Detection of PARP14 protein in untreated (−) and LPS-treated RAW 264.7 macrophages. Upper panel, Total lysates; lower panel, cytosolic and nuclear distribution. Vinculin, lamin, and tubulin are shown as loading controls. UT, untreated.

We next applied CRISPR/Cas9–mediated genome editing to knock out *Parp14* in RAW 264.7 macrophages. Specifically, we used a single-guide RNA designed on the first exon of the *Parp14* gene, which caused both small mutations and big deletions on different alleles of four selected clones (sequences details in Supplemental Table III). We next employed a pool of these four *Parp14* KO clones to determine the consequences of PARP14 absence. The expression of both the PARP14 protein (Fig. 3A, left panel) and mRNA (Fig. 3A, right panel) was completely abrogated, both before and after LPS stimulation. PARP14 deletion nearly completely abrogated LPS-induced nuclear translocation of four out of six interactors tested (NMI, IFI35, DTX3L, and PARP9), whereas p62 and PARP12 nuclear localization was only mildly affected (Fig. 3B). In agreement with that, we observed that NMI and IFI35 nuclear translocation was similarly attenuated also in PARP14$^{-/-}$ BMDMs, although the effect was of more limited magnitude than in RAW 264.7 cells (Fig. 3C).

Effects of PARP14 depletion on the LPS response

LPS binding to TLR4 induces the activation of several primary response genes, including a small panel of five genes directly controlled by the transcription factor IRF3 (53) such as *Ifnb1* and *Ccl5*. Secreted IFN-β binds to the IFN-α/β receptor (IFNAR1/2),

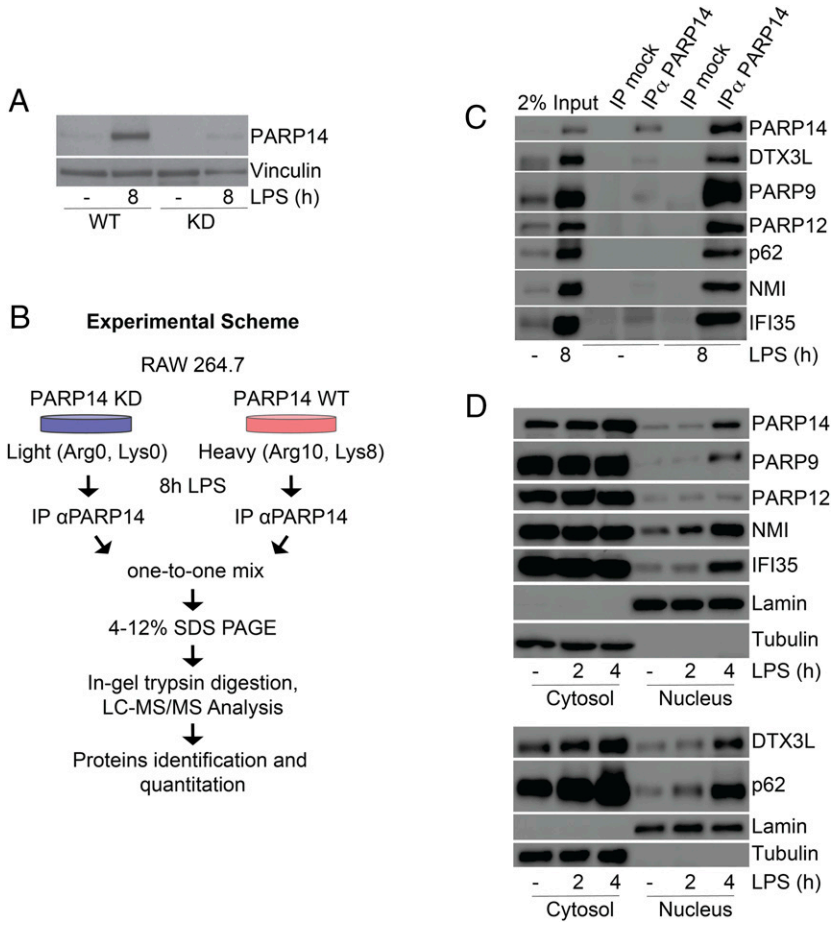

FIGURE 2. SILAC-based MS analysis and coimmunoprecipitation validation of PARP14 interactors. (**A**) shRNA-mediated knockdown of PARP14 protein (shRNA no. 1) in untreated (−) and LPS-treated RAW 264.7 cells. Vinculin is shown as loading control. (**B**) PARP14-depleted and WT RAW 264.7 cells were grown in heavy and light SILAC media, respectively; upon full SILAC amino acid incorporation, both cells were treated with LPS, harvested, and nuclear extracts were prepared, which were used as input in two parallel anti-PARP14 coimmunoprecipitation experiments. The two immunoprecipitates were mixed in a one-to-one ratio, and proteins were eluted, separated by SDS-PAGE, and then subjected to in-gel trypsin digestion followed by LC-MS/MS analysis for protein identification and quantitation. (**C**) LPS-treated RAW 264.7 macrophages lysates were immunoprecipitated with anti-PARP14 Ab or control (rabbit IgG) and immunoblotted as indicated. A fraction of the input lysate is shown on the left. (**D**) Cytosolic and nuclear distribution of PARP14 and PARP14-bound ISG-encoded proteins in untreated and LPS-treated RAW 264.7 macrophages. Lamin and tubulin are shown as loading controls. IP, immunoprecipitation.

triggering phosphorylation and activation of the STAT1/STAT2/IRF9 trimeric complex and, to a lesser extent, STAT1 homodimers (29), which translocate to the nucleus and initiate transcription of secondary antiviral response genes (73). To investigate the role of PARP14 in the transcriptional response to LPS, we performed an RNA-seq analysis in WT and PARP14 KO RAW 264.7 cells. We

Table IV. A subset of the best PARP14-specific interactors on the basis of their normalized SILAC $\log_2$ heavy to light ratio (H/L) as top 10% of the distribution

Protein Names	Gene Names	Peptides	Unique Peptides	Ratio H/L Normalized	Log2 (Ratio H/L Normalized)	Ratio H/L Count
Tripartite motif-containing protein 7	*Trim7*	1	1	20.92	4.39	2
PARP14	*Parp14*	109	109	17.088	4.09	308
PARP9	*Parp9*	13	13	16.108	4.01	9
E3 ubiquitin-protein ligase DTX3L	*Dtx3l*	2	2	14.223	3.83	2
Polyubiquitin-C	*Ubc*	5	5	12.122	3.60	25
PARP12	*Parp12*	7	7	11.509	3.52	3
SQSTM1	*Sqstm1*	9	9	8.0593	3.01	6
Phosphate carrier protein, mitochondrial	*Slc25a3*	2	2	7.0496	2.82	3
N-myc-interactor	*Nmi*	9	9	5.4132	2.44	5
Dolichyl-diphosphooligo-saccharide-subunit 2	*Rpn2*	3	3	4.2341	2.08	2

The subset of interactors was selected from Supplemental Table II. PARP14 is highlighted in blue; IFN-stimulated proteins are highlighted in red.

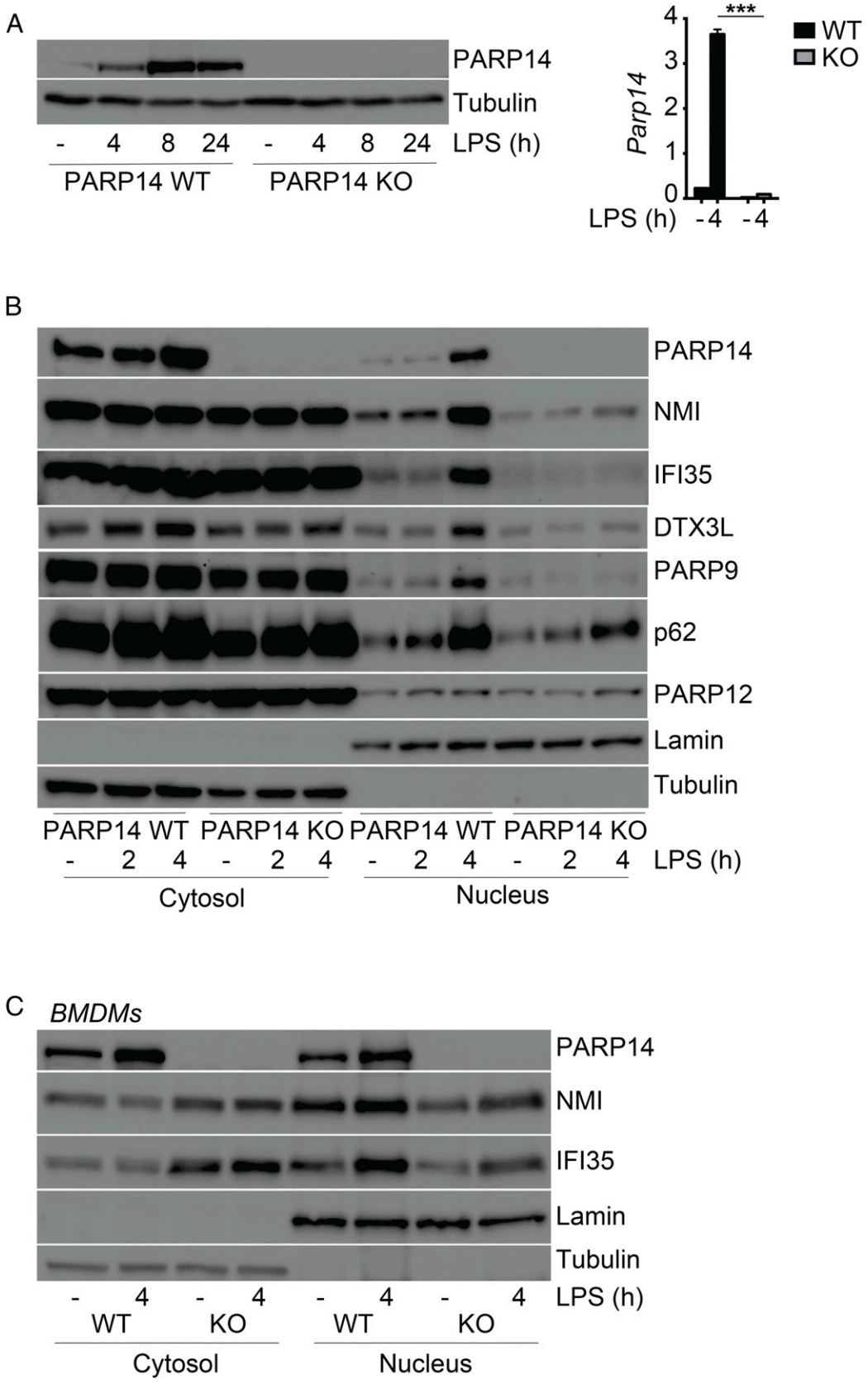

FIGURE 3. PARP14 is essential to enable ISG-encoded proteins nuclear translocation. (**A**) Left panel, CRISPR/Cas9-mediated PARP14 KO in RAW 264.7 cells, untreated (−) or LPS treated. Tubulin is shown as loading control. Right panel, Kinetics of *Parp14* mRNA levels in PARP14 WT and KO RAW 264.7 macrophages upon LPS treatment. Data are displayed as ratio to the *TBP* mRNA. Data represent the mean of three independent experiments each performed in triplicate ($n = 3$). Significance was determined by two-way ANOVA with a Sidak's posttest. ***$p < 0.001$. (**B**) Cytosolic and nuclear distribution of PARP14 and PARP14-bound ISG-encoded proteins in PARP14 WT and KO RAW 264.7 macrophages upon LPS treatment. Lamin and tubulin are shown as loading controls. (**C**) Cytosolic and nuclear distribution of PARP14, NMI, and IFI35 proteins in PARP14 WT and KO primary BMDMs upon LPS treatment. Lamin and tubulin are shown as loading controls.

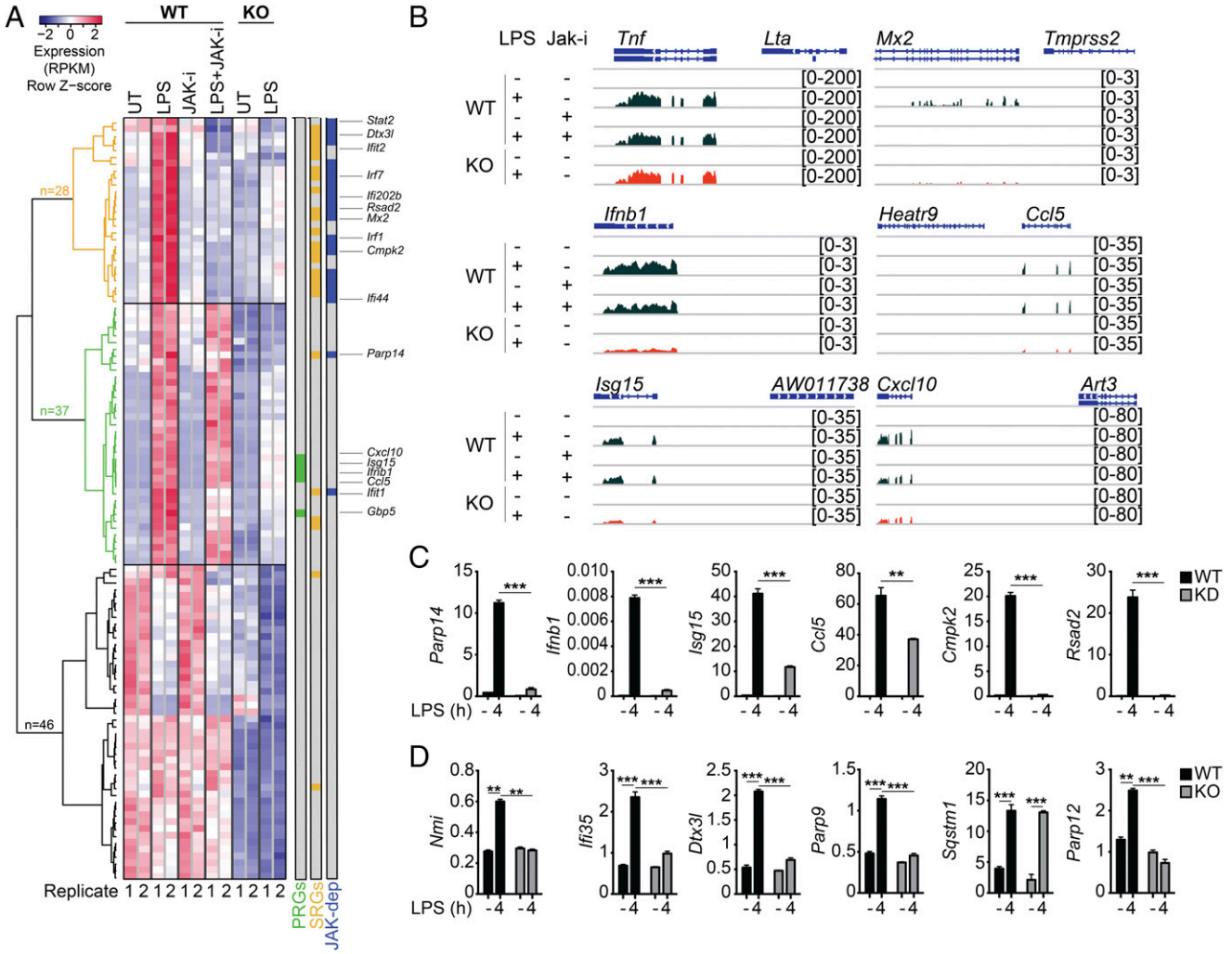

FIGURE 4. PARP14 depletion affects the expression of primary and secondary antiviral response genes. (**A**) Heat map showing the mRNA of 111 genes differentially expressed in PARP14 WT or KO RAW 264.7 macrophages upon LPS, JAK inhibitor (JAK-i), or LPS plus JAK inhibitor (LPS+JAK-i) treatment (FDR $\leq$ 0.01, 2-fold, RPKM $\geq$ 1). Some of the most significant inflammation-related genes are indicated. The color bar indicates the intensity of gene expression (red indicates highly expressed genes; blue indicates lowly expressed genes). Rows were hierarchically clustered using the complete-linkage method as algorithm and the Pearson correlation as distance metric. Green, yellow, and black branches indicate three hierarchical clusters that include 37, 28 and 46 genes, respectively. PRGs, in green, and SRGs, in yellow, are flagged according to their functional classification in the literature (53); JAK-dependent genes are flagged in blue (FDR $\leq$ 0.01, 2-fold). (**B**) Five representative RNA-seq snapshots showing the effect of PARP14 depletion on some PRGs (*Mx2*) and SRGs (*Ifnb1*, *Ccl5*, *Isg15*, and *Cxcl10*) upon the indicated treatments. *Tnf* is shown as negative control. (**C**) RAW 264.7 clones stably harboring shRNAs (shRNA no. 2) specific for PARP14 are compromised in the expression of some primary and secondary antiviral response genes as shown by the mRNA expression of *Parp14*, *Ifnb1*, *Isg15*, *Ccl5*, *Cmpk2*, and *Rsad2* in PARP14 WT and knockdown (KD) RAW 264.7 macrophages upon LPS treatment. Data are displayed as ratio to the *TBP* mRNA. Data represent the mean of three independent experiments each performed in triplicate ($n = 3$). Significance was determined by two-way ANOVA with a Sidak posttest. $^{**}p < 0.01$, $^{***}p < 0.001$. (**D**) mRNA expression of the six PARP14-bound ISGs, in PARP14 WT and KO RAW 264.7 macrophages, upon 4 h LPS treatment. Data are displayed as ratio to the *TBP* mRNA. Data represent the mean of three independent experiments each performed in triplicate ($n = 3$). Significance was determined by a two-way ANOVA with a Sidak posttest and Student *t* test. $^{***}p < 0.01$, $^{**}p < 0.001$. JAK-dep, JAK-dependent genes.

compared untreated and LPS-treated cells and, to directly identify secondary genes activated downstream of IFN-β receptor triggering, we used the selective inhibitor of the JAKs (JAK inhibitor I, CAS 457081-03-7), which possesses inhibitory activity toward JAK1, JAK2, JAK3, and tyrosine kinase 2. Deletion of *Parp14* caused a robust decrease in transcription of a small number of primary response genes, including IRF3-dependent genes (*Ifnb1*, *Ccl5*, *Isg15*, and *Cxcl10)* (53) and of a large fraction of the secondary IFN-β–dependent genes (such as *Mx2*) (Fig. 4A). Representative snapshots are shown in Fig. 4B. To validate these results using an independent experimental setup, we generated RAW 264.7 macrophage clones stably harboring shRNAs specific for PARP14 (shRNA no. 2). Also in these PARP14-depleted cells we observed a similar impairment of LPS-inducible gene expression (Fig. 4C). Finally, the mRNA of the PARP14 interactors *Nmi*, *Ifi35*, *Dtx3l*, *Parp9*, and *Parp12* were induced by LPS stimulation in a PARP14-dependent manner, whereas *Sqstm1* mRNA was upregulated even in a PARP14 KO background (Fig. 4D).

Expression and phosphorylation of IRF3, both in total lysates and in the cytosolic and nuclear compartments, were unaffected by PARP14 absence (Fig. 5A, upper and middle panels), implying that defective IRF3-dependent transcription occurred downstream of its phosphorylation and nuclear translocation. In agreement with the transcriptional data presented above, we detected a

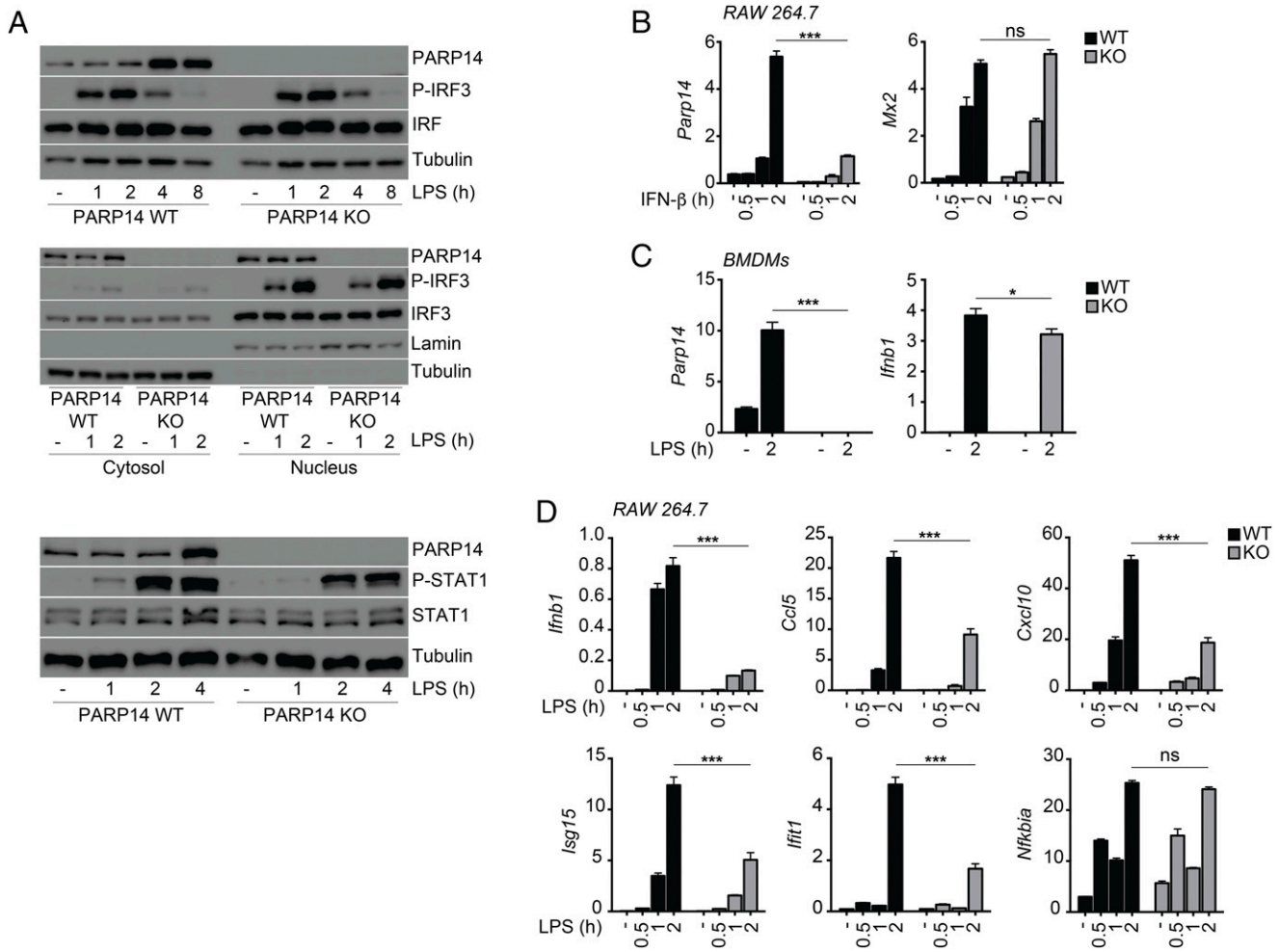

FIGURE 5. Lack of PARP14 hampered the inducible transcription of *Ifnb1* gene affecting STAT1 phosphorylation, thus altering ISG expression. (**A**) IRF3 total and phosphorylation levels, upon LPS treatment, in PARP14 WT and KO RAW 264.7 macrophages (upper panel); cytosolic and nuclear distribution of IRF3 total and phosphorylation levels, upon LPS treatment, in PARP14 WT and KO RAW 264.7 macrophages (middle panel). STAT1 total and phosphorylation levels, upon LPS treatment, in PARP14 WT and KO RAW 264.7 macrophages (lower panel). Tubulin and lamin are shown as loading controls. (**B**) mRNA expression of *Mx2* in PARP14 WT and KO RAW 264.7 macrophages demonstrates that PARP14 depletion does not affect the transcription of IFN-inducible genes upon IFN-β stimulation. Data are displayed as ratio to the *TBP* mRNA. Data represent the mean of three independent experiments each performed in triplicate ($n = 3$). Significance was determined by two-way ANOVA with a Sidak posttest. $***p < 0.001$. (**C**) The KO of PARP14, in primary BMDMs, mildly affected IFN-β transcription, upon LPS treatment, as illustrated by the kinetics of *Ifnb1* mRNA expression in PARP14 WT and KO primary BMDMs. Data represent the mean of two independent experiments each performed in triplicate ($n = 3$). Significance was determined by two-way ANOVA with a Sidak posttest. $*p \leq 0.05$, $***p < 0.001$. (**D**) Nascent mRNA expression of five IRF3-regulated genes in PARP14 WT and KO RAW 264.7 macrophages upon LPS treatment. *Nfkbia* is shown as negative control. Data are displayed as ratio to the *TBP* mRNA. Data represent the mean of three independent experiments each performed in triplicate ($n = 3$). Significance was determined by two-way ANOVA with a Sidak posttest. $***p < 0.001$. ns, not significant.

decrease in the LPS-induced phosphorylation of STAT1 in *Parp14* KO cells compared with their WT counterpart (Fig. 5A, lower panel). However, PARP14 KO cells were normally sensitive to exogenous IFN-β stimulation, suggesting that the observed defects in the expression of ISGs in *Parp14* KO cells could not be attributed to an impaired IFN-β response (Fig. 5B) but rather to a decrease in *Ifnb1* gene transcription. Finally, we analyzed *Ifnb1* transcription in *Parp14* null primary BMDMs. Compared to RAW 264.7 cells, the reduction of *Ifnb1* gene expression was of much lower magnitude (Fig. 5C), suggesting that other regulators of *Ifnb1* transcription might compensate for the lack of *Parp14* in primary cells. Overall, these results suggest that PARP14 can contribute to transcriptional regulation of *Ifnb1* and other IRF3-dependent genes activated in response to LPS.

We have shown above that PARP14 binds to and allows the nuclear translocation of NMI, an IFN-inducible protein previously implicated in transcriptional control (71). To determine whether NMI contributes to transcriptional regulation of LPS-activated genes, we used CRISPR/Cas9-mediated genome editing to generate NMI KO clones in RAW 264.7 cells. NMI deletion abrogated the protein expression of IFI35, but not mRNA (data not shown), a result consistent with a mutual requirement of the two proteins for reciprocal stabilization in the heterodimer (Supplemental Fig. 1A). Instead, protein levels of PARP14 (Supplemental Fig. 1A) and its subcellular localization after endotoxin stimulation (Supplemental Fig. 1B) were unaffected by NMI loss. Moreover, *Nmi* null RAW 264.7 macrophages expressed normal amounts of *Parp14* and *Ifnb1* mRNA after LPS treatment (Supplemental Fig. 1C). Consistent with this result, the mRNA expression of other classical inflammatory genes was not significantly different in WT and *Nmi* null cells (Supplemental Fig. 1D). These data suggest that NMI, whose nuclear accumulation requires PARP14, does not participate in the transcriptional regulation of *Ifnb1* and other

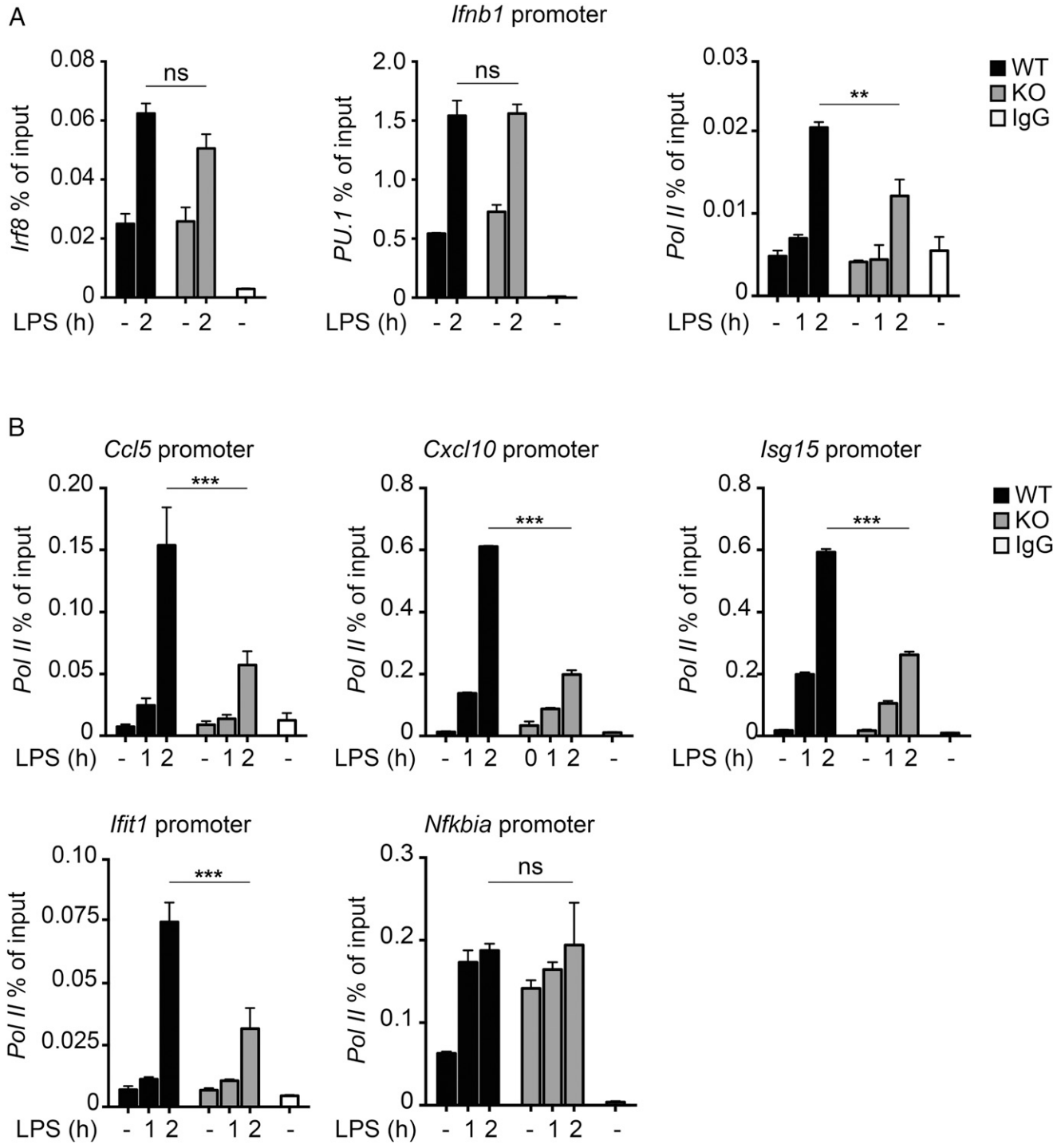

FIGURE 6. Effects of PARP14 depletion on transcription factors recruitment on promoters of IRF3-regulated genes. (**A**) IRF8, PU.1, and Pol II recruitment on *Ifnb1* promoter in PARP14 WT and KO RAW 264.7 macrophages upon LPS treatment. (**B**) Pol II recruitment on *Ccl5*, *Cxcl10*, *Isg15*, and *Ifit1* promoters in PARP14 WT and KO RAW 264.7 macrophages upon LPS treatment. *Nfkbia* is shown as negative control. Data represent the mean of three independent experiments each performed in triplicate ($n = 3$). Significance was determined by two-way ANOVA with a Sidak posttest. $^{**}p < 0.01$, $^{***}p < 0.001$. ns, not significant.

IRF3-dependent genes activated in response to endotoxin treatment.

PARP14 controls RNA Pol II recruitment to the promoters of IRF3-regulated genes

To clarify the mechanisms linking PARP14 loss to changes in LPS-induced gene expression, we analyzed nascent transcripts by 4sU labeling in *Parp14* KO RAW 264.7 cells and their WT counterpart. qPCR analysis of nascent RNAs showed that the lack of PARP14 strongly attenuated the inducible transcription of *Ifnb1* and the other IRF3-regulated genes tested (Fig. 5D), indicating that reduced expression of these genes occurred at the transcriptional level. We next analyzed the recruitment to the *Ifnb1* and other IRF3-dependent genes promoters of selected transcription factors before and after LPS stimulation. Possibly due to limitations of the available Abs, we could not obtain an

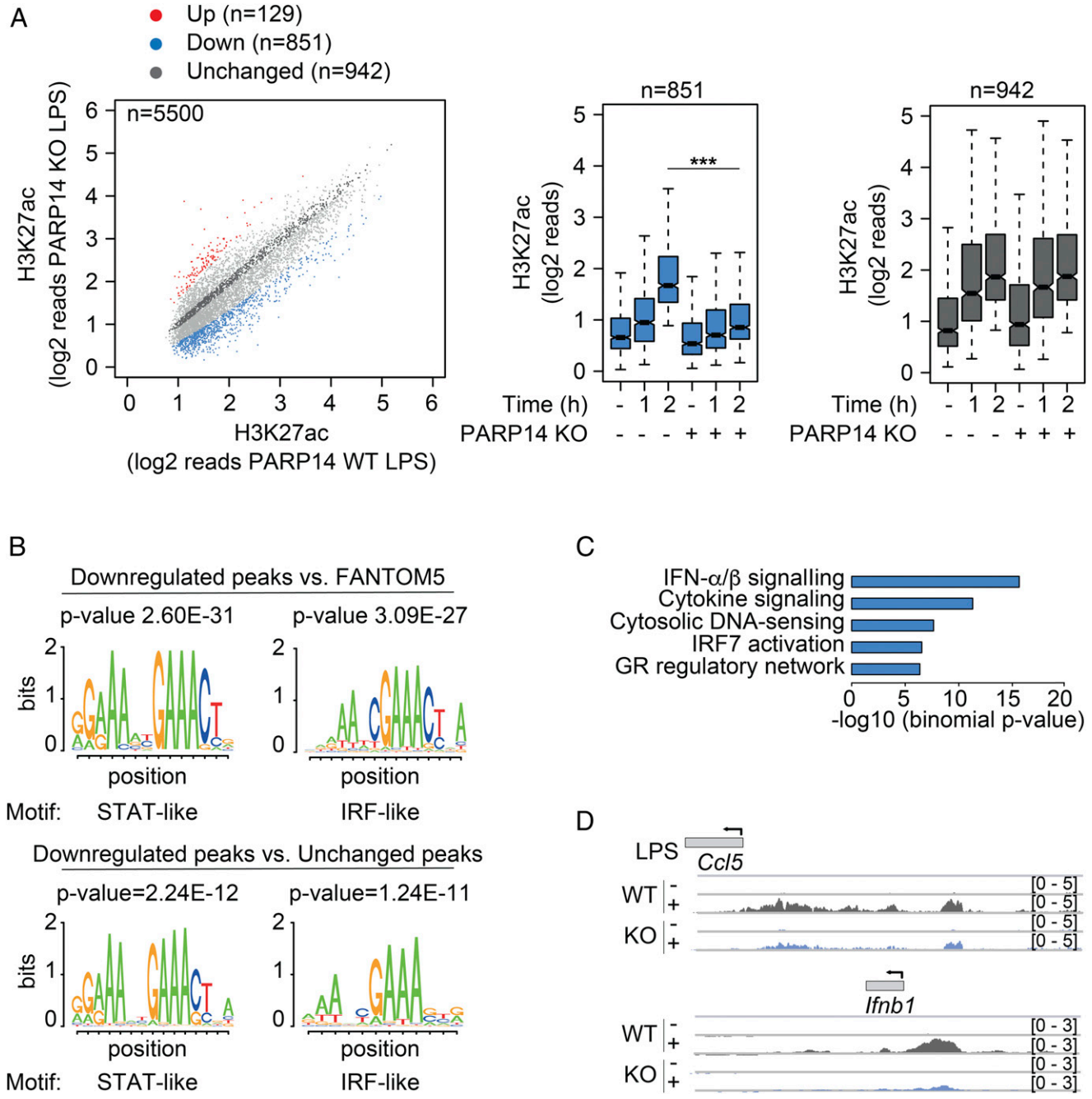

FIGURE 7. PARP14 deficiency affects H3K27 acetylation of promoters regulating genes involved in the endotoxin response. (**A**) Left panel, Scatterplot indicating H3K27ac genomic normalized read counts, $\log_2$ transformed, in 2 h LPS-treated PARP14 KO RAW 264.7 macrophages relative to WT cells. Differentially acetylated regions are represented by red (increased), blue (reduced), and dark gray (unchanged) dots. Right panel, Box plots illustrating the downregulated (left) and unchanged (right) acetylation signals in *Parp14* null versus WT cells upon 0, 1, and 2 h LPS treatment. Significance was determined by a Wilcoxon rank sum test. ***$p < 0.001$. (**B**) Transcription factor motifs (STAT/IRF DNA-binding motifs) found overrepresented in the PARP14-dependent H3K27ac downregulated genomic peaks 2 h after LPS stimulus. (**C**) Selected genome ontology categories enriched in the sets of H3K27ac downregulated genomic regions, according to GREAT v3.0.0. GR, glucocorticoid receptor. (**D**) Two representative ChIP-seq snapshots showing the effects of PARP14 deficiency on H3K27 acetylation levels on promoters of genes involved in the response to LPS.

anti-IRF3 ChIP. IRF8 and PU.1 form a complex assisting IRF3 activity at the *Ifnb1* gene promoter (29), and their recruitment was not altered in *Parp14* null macrophages. However, we observed a significant decrease in RNA Pol II recruitment after LPS treatment (Fig. 6A). In agreement with that, LPS-induced RNA Pol II association with other IRF3-dependent gene promoters was also strongly impaired in PARP14-depleted cells (Fig. 6B).

Effects of PARP14 deficiency on genomic H3K27 acetylation

H3K27ac is a hallmark of active promoters and enhancers (37, 44). Gains or losses of histone acetylation signals are informative of underlying regulatory events, as they reflect changes in binding or activity of sequence-specific transcription factors (74, 75). To determine whether PARP14 deficiency had additional consequences other than impairing the secondary IFN-β1 response, we analyzed the impact of PARP14 absence on H3K27ac genomic

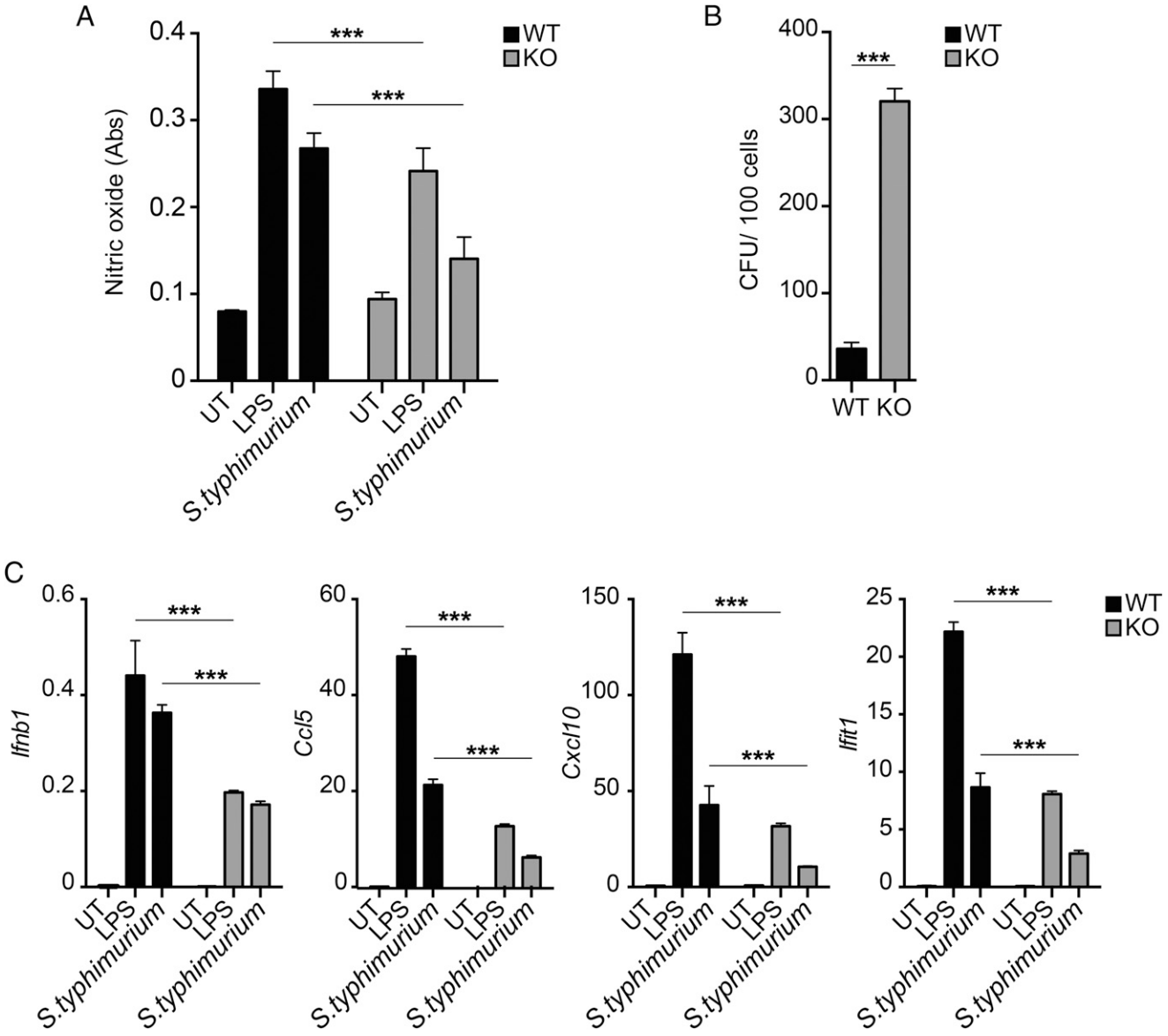

FIGURE 8. *Parp14* null RAW 264.7 macrophages are more susceptible to microbial attack. (**A**) NO production by PARP14 WT and KO RAW 264.7 macrophages upon LPS treatment and *S. typhimurium* infection. NO quantification was assessed 24 h after *S. typhimurium* infection. Data represent the mean of three independent experiments each performed in triplicate ($n = 3$). Significance was determined by two-way ANOVA with a Sidak posttest. $^{***}p < 0.001$. (**B**) Bacterial counts from PARP14 WT and KO RAW 264.7 macrophages 7 h after *S. typhimurium* infection. Cells were harvested, lysed, and plated overnight on agar plates to evaluate bacterial invasion. Data represent the mean of three independent experiments each performed in quadruplicate ($n = 4$). Significance was determined by a Student *t* test. $^{***}p < 0.001$. (**C**) Kinetics of *Ifnb1*, *Ccl5*, *Cxcl10*, and *Ifit1* mRNA expression in PARP14 WT and KO RAW 264.7 cells upon 4 h LPS treatment or *S. typhimurium* infection. Data are displayed as ratio to the *TBP* mRNA. Data represent the mean of two independent experiments each performed in triplicate ($n = 3$). Significance was determined by two-way ANOVA with a Sidak posttest. $^{***}p < 0.001$.

distribution using ChIP-seq in WT and *Parp14* KO RAW 264.7 cells, before and after LPS stimulation. Eight hundred fifty-one genomic regions showed a significantly reduced H3K27ac signal after 2 h of LPS treatment in *Parp14* null cells compared with their WT controls (Fig. 7A). Consistent with the impaired IFN-β1 response in PARP14-deficient cells, the genomic regions associated with the downregulated peaks showed a statistically significant overrepresentation of STAT/IRF DNA-binding motifs (Fig. 7B). Moreover, when considering the genes associated with the genomic regions showing deregulated H3K27ac peaks, we retrieved mainly ontology terms related to IFN and cytokine signaling (Fig. 7C). Importantly, the same type of analyses did not allow us to identify changes in the activity of other signal-regulated transcription factors, suggesting that in this context the effects of PARP14 were restricted to the defective activation of IRF3 targets and particularly IFN-β1, eventually resulting in a global reduction in the activity of IFN-β1–stimulated genomic regulatory elements. Representative H3K27ac peak distributions, along the genomic regions of two classical IRF3-dependent genes, are shown in Fig. 7D.

RAW 264.7 macrophages lacking PARP14 are more sensitive to S. typhimurium *infection*

The data shown above hint at a possible role for PARP14 in the antimicrobial defense. To test this possibility, we analyzed *S. typhimurium* infection in PARP14 WT and KO RAW 264.7 macrophages. This pathogen expresses multiple pathogen-associated molecular patterns, including LPS and flagellin, that strongly stimulate TLR4 and NLRC4, respectively, inducing the expression of type I IFN (76, 77). The *S. typhimurium* WT invasive

strain (in SL1344 background) was used to infect RAW 264.7 cells. After infection, cells were washed and medium containing gentamicin was maintained throughout the experiments to kill any extracellular bacteria. After 24 h, culture supernatants were collected and nitrite accumulation was measured. We observed that both after LPS treatment and *S. typhimurium* infection, PARP14 KO cells were impaired in NO production as compared with their WT counterparts (Fig. 8A). To measure bacterial replication in the absence of PARP14, CFU levels were measured after 7 h of infection in WT and KO RAW 264.7 macrophages. Intracellular *S. typhimurium* CFU levels were significantly higher in PARP14 KO cells (Fig. 8B). In keeping with these results, we observed that in cells lacking PARP14, the expression of IRF3-dependent genes, in response to *S. typhimurium* infection, was impaired (Fig. 8C).

Discussion

Previous studies suggested the involvement of various PARPs (including PARP7, PARP9, PARP10, PARP12, and PARP13) in inflammatory responses and host defense against infections, dependent or not on their enzymatic activity (12–14, 18, 19). Moreover, it has been recently shown that the macro-domain of the Chikungunya virus encodes an ADP-ribo-hydrolase whose activity is essential for virulence (78), thus indicating a biological role for the removal of mono-ADP-ribose units.

Our observation that more than half of the PARP superfamily genes were strongly upregulated upon LPS treatment of BMDMs is consistent with these previous findings. Nevertheless, the role played by most of these genes in the inflammatory response is still largely unknown. A recent study on macrophage activation upon IFN-γ and IL-4 stimulation reported opposing roles for PARP14 and PARP9, with PARP14 absence promoting a proinflammatory outcome and STAT1 hyperphosphorylation, and PARP9 depletion, instead, attenuating inflammatory gene expression (79).

In our study, we found a previously uncharacterized function for PARP14 in regulating the IFN-β response in murine macrophages. Specifically, upon endotoxin stimulation PARP14 bound to a group of ISG-encoded proteins, and it enabled their nuclear accumulation. Moreover, PARP14 loss attenuated transcription of IRF3-regulated primary response genes, thus reducing both IFN-β production and activation of genes involved in the secondary antiviral response, although the magnitude of this effect was limited in primary BMDMs compared with RAW 264.7 cells. Two ISG-encoded proteins bound by PARP14, the E3 ligase DTX3L and PARP9, possess an IFN-γ–responsive bidirectional promoter (12) and once bound together they act as a STAT1-associated component of type I IFNR signal transduction, thus promoting ISG expression (13). The IFN inducible PARP12 was previously identified as a broad-spectrum antiviral protein (18, 19) and SWSTM1/p62, a multifunctional scaffold protein, also participates in regulation of inflammation (64–66). Interestingly, another IFN-stimulated protein, NMI (68), which was reported to potentiate STAT1- and STAT5-dependent transcription (71), also efficiently interacted with PARP14 in the nuclear compartment. NMI was described to form a stable high–molecular mass complex with the IFN-stimulated protein IFI35 (67, 69, 70), which was reported to control AP-1–mediated gene transcription (72). We demonstrated that also IFI35 was strongly bound to nuclear PARP14 after LPS treatment. In line with the results obtained with the SILAC-based MS and the coimmunoprecipitation experiments, we observed that PARP14 and its binding partners showed a similar trend in terms of cytosolic and nuclear distribution, before and after LPS stimulation. Most importantly, the nuclear accumulation of these IFN-stimulated proteins was strongly reduced in cells lacking PARP14. This unexpected role for PARP14 in the regulation of the nuclear accumulation of a selected group of IFN-stimulated proteins hints at a possible involvement of this PARP in the control of pathogens replicating in the nucleus (80, 81). In agreement with these data, PARP14 hindered *S. typhimurium* proliferation in macrophages. Moreover, after infection, PARP14 KO macrophages showed lower NO production and impaired transcription of IRF3-regulated primary response genes, which likely contributed to the higher bacterial load. Collectively, our data suggest a role for murine PARP14 in controlling the IFN response, both by regulating the mRNA expression of primary and secondary antiviral response genes, and by enforcing the nuclear accumulation of a small group of specific ISG-encoded proteins.

Acknowledgments

We thank Francesca Algieri (Center for Biomedical Research, University of Granada, Granada, Spain), Chiara Pozzi (European Institute of Oncology, Milan, Italy), and Giuseppe Penna (European Institute of Oncology, Milan, Italy) for scientific support and discussion.

Disclosures

The authors have no financial conflicts of interest.

References

1. Schreiber, V., F. Dantzer, J. C. Ame, and G. de Murcia. 2006. Poly(ADP-ribose): novel functions for an old molecule. *Nat. Rev. Mol. Cell Biol.* 7: 517–528.
2. Hottiger, M. O., P. O. Hassa, B. Lüscher, H. Schüler, and F. Koch-Nolte. 2010. Toward a unified nomenclature for mammalian ADP-ribosyltransferases. *Trends Biochem. Sci.* 35: 208–219.
3. Berger, F., M. H. Ramírez-Hernández, and M. Ziegler. 2004. The new life of a centenarian: signalling functions of NAD(P). *Trends Biochem. Sci.* 29: 111–118.
4. Aguiar, R. C., Y. Yakushijin, S. Kharbanda, R. Salgia, J. A. Fletcher, and M. A. Shipp. 2000. BAL is a novel risk-related gene in diffuse large B-cell lymphomas that enhances cellular migration. *Blood* 96: 4328–4334.
5. Aguiar, R. C., K. Takeyama, C. He, K. Kreinbrink, and M. A. Shipp. 2005. B-aggressive lymphoma family proteins have unique domains that modulate transcription and exhibit poly(ADP-ribose) polymerase activity. *J. Biol. Chem.* 280: 33756–33765.
6. Kleine, H., E. Poreba, K. Lesniewicz, P. O. Hassa, M. O. Hottiger, D. W. Litchfield, B. H. Shilton, and B. Lüscher. 2008. Substrate-assisted catalysis by PARP10 limits its activity to mono-ADP-ribosylation. *Mol. Cell* 32: 57–69.
7. Berger, M. F., G. Badis, A. R. Gehrke, S. Talukder, A. A. Philippakis, L. Peña-Castillo, T. M. Alleyne, S. Mnaimneh, O. B. Botvinnik, E. T. Chan, et al. 2008. Variation in homeodomain DNA binding revealed by high-resolution analysis of sequence preferences. *Cell* 133: 1266–1276.
8. Goenka, S., and M. Boothby. 2006. Selective potentiation of Stat-dependent gene expression by collaborator of Stat6 (CoaSt6), a transcriptional cofactor. *Proc. Natl. Acad. Sci. USA* 103: 4210–4215.
9. Goenka, S., S. H. Cho, and M. Boothby. 2007. Collaborator of Stat6 (CoaSt6)-associated poly(ADP-ribose) polymerase activity modulates Stat6-dependent gene transcription. *J. Biol. Chem.* 282: 18732–18739.
10. Mehrotra, P., J. P. Riley, R. Patel, F. Li, L. Voss, and S. Goenka. 2011. PARP-14 functions as a transcriptional switch for Stat6-dependent gene activation. *J. Biol. Chem.* 286: 1767–1776.
11. Iqbal, M. B., M. Johns, J. Cao, Y. Liu, S. C. Yu, G. D. Hyde, M. A. Laffan, F. P. Marchese, S. H. Cho, A. R. Clark, et al. 2014. PARP-14 combines with tristetraprolin in the selective posttranscriptional control of macrophage tissue factor expression. *Blood* 124: 3646–3655.
12. Juszczynski, P., J. L. Kutok, C. Li, J. Mitra, R. C. Aguiar, and M. A. Shipp. 2006. BAL1 and BBAP are regulated by a γ interferon-responsive bidirectional promoter and are overexpressed in diffuse large B-cell lymphomas with a prominent inflammatory infiltrate. *Mol. Cell. Biol.* 26: 5348–5359.
13. Zhang, Y., D. Mao, W. T. Roswit, X. Jin, A. C. Patel, D. A. Patel, E. Agapov, Z. Wang, R. M. Tidwell, J. J. Atkinson, et al. 2015. PARP9-DTX3L ubiquitin ligase targets host histone H2BJ and viral 3C protease to enhance interferon signaling and control viral infection. *Nat. Immunol.* 16: 1215–1227.
14. Gao, G., X. Guo, and S. P. Goff. 2002. Inhibition of retroviral RNA production by ZAP, a CCCH-type zinc finger protein. *Science* 297: 1703–1706.
15. Kerns, J. A., M. Emerman, and H. S. Malik. 2008. Positive selection and increased antiviral activity associated with the PARP-containing isoform of human zinc-finger antiviral protein. *PLoS Genet.* 4: e21.
16. Chen, G., X. Guo, F. Lv, Y. Xu, and G. Gao. 2008. p72 DEAD box RNA helicase is required for optimal function of the zinc-finger antiviral protein. *Proc. Natl. Acad. Sci. USA* 105: 4352–4357.
17. Zhu, Y., and G. Gao. 2008. ZAP-mediated mRNA degradation. *RNA Biol.* 5: 65–67.

18. Liu, S. Y., D. J. Sanchez, R. Aliyari, S. Lu, and G. Cheng. 2012. Systematic identification of type I and type II interferon-induced antiviral factors. *Proc. Natl. Acad. Sci. USA* 109: 4239–4244.
19. Atasheva, S., M. Akhrymuk, E. I. Frolova, and I. Frolov. 2012. New PARP gene with an anti-alphavirus function. *J. Virol.* 86: 8147–8160.
20. Hargreaves, D. C., T. Horng, and R. Medzhitov. 2009. Control of inducible gene expression by signal-dependent transcriptional elongation. *Cell* 138: 129–145.
21. De Santa, F., V. Narang, Z. H. Yap, B. K. Tusi, T. Burgold, L. Austenaa, G. Bucci, M. Caganova, S. Notarbartolo, S. Casola, et al. 2009. Jmjd3 contributes to the control of gene expression in LPS-activated macrophages. *EMBO J.* 28: 3341–3352.
22. Cho, S. H., S. Goenka, T. Henttinen, P. Gudapati, A. Reinikainen, C. M. Eischen, R. Lahesmaa, and M. Boothby. 2009. PARP-14, a member of the B aggressive lymphoma family, transduces survival signals in primary B cells. *Blood* 113: 2416–2425.
23. Dickins, R. A., M. T. Hemann, J. T. Zilfou, D. R. Simpson, I. Ibarra, G. J. Hannon, and S. W. Lowe. 2005. Probing tumor phenotypes using stable and regulated synthetic microRNA precursors. [Published erratum appears in 2006 *Nat. Genet.* 38: 389.] *Nat. Genet.* 37: 1289–1295.
24. Ran, F. A., P. D. Hsu, J. Wright, V. Agarwala, D. A. Scott, and F. Zhang. 2013. Genome engineering using the CRISPR-Cas9 system. *Nat. Protoc.* 8: 2281–2308.
25. Sanjana, N. E., O. Shalem, and F. Zhang. 2014. Improved vectors and genome-wide libraries for CRISPR screening. *Nat. Methods* 11: 783–784.
26. Rabani, M., J. Z. Levin, L. Fan, X. Adiconis, R. Raychowdhury, M. Garber, A. Gnirke, C. Nusbaum, N. Hacohen, N. Friedman, et al. 2011. Metabolic labeling of RNA uncovers principles of RNA production and degradation dynamics in mammalian cells. *Nat. Biotechnol.* 29: 436–442.
27. Ding, A. H., C. F. Nathan, and D. J. Stuehr. 1988. Release of reactive nitrogen intermediates and reactive oxygen intermediates from mouse peritoneal macrophages. Comparison of activating cytokines and evidence for independent production. *J. Immunol.* 141: 2407–2412.
28. Austenaa, L., I. Barozzi, A. Chronowska, A. Termanini, R. Ostuni, E. Prosperini, A. F. Stewart, G. Testa, and G. Natoli. 2012. The histone methyltransferase Wbp7 controls macrophage function through GPI glycolipid anchor synthesis. *Immunity* 36: 572–585.
29. Mancino, A., A. Termanini, I. Barozzi, S. Ghisletti, R. Ostuni, E. Prosperini, K. Ozato, and G. Natoli. 2015. A dual *cis*-regulatory code links IRF8 to constitutive and inducible gene expression in macrophages. *Genes Dev.* 29: 394–408.
30. Langmead, B., and S. L. Salzberg. 2012. Fast gapped-read alignment with Bowtie 2. *Nat. Methods* 9: 357–359.
31. Zang, C., D. E. Schones, C. Zeng, K. Cui, K. Zhao, and W. Peng. 2009. A clustering approach for identification of enriched domains from histone modification ChIP-Seq data. *Bioinformatics* 25: 1952–1958.
32. Jolma, A., J. Yan, T. Whitington, J. Toivonen, K. R. Nitta, P. Rastas, E. Morgunova, M. Enge, M. Taipale, G. Wei, et al. 2013. DNA-binding specificities of human transcription factors. *Cell* 152: 327–339.
33. Robinson, M. D., D. J. McCarthy, and G. K. Smyth. 2010. edgeR: a bioconductor package for differential expression analysis of digital gene expression data. *Bioinformatics* 26: 139–140.
34. Robinson, M. D., and G. K. Smyth. 2008. Small-sample estimation of negative binomial dispersion, with applications to SAGE data. *Biostatistics* 9: 321–332.
35. McCarthy, D. J., Y. Chen, and G. K. Smyth. 2012. Differential expression analysis of multifactor RNA-Seq experiments with respect to biological variation. *Nucleic Acids Res.* 40: 4288–4297.
36. Barski, A., S. Cuddapah, K. Cui, T. Y. Roh, D. E. Schones, Z. Wang, G. Wei, I. Chepelev, and K. Zhao. 2007. High-resolution profiling of histone methylations in the human genome. *Cell* 129: 823–837.
37. Wang, Z., C. Zang, J. A. Rosenfeld, D. E. Schones, A. Barski, S. Cuddapah, K. Cui, T. Y. Roh, W. Peng, M. Q. Zhang, and K. Zhao. 2008. Combinatorial patterns of histone acetylations and methylations in the human genome. *Nat. Genet.* 40: 897–903.
38. ENCODE Project Consortium. 2012. An integrated encyclopedia of DNA elements in the human genome. *Nature* 489: 57–74.
39. Hinrichs, A. S., D. Karolchik, R. Baertsch, G. P. Barber, G. Bejerano, H. Clawson, M. Diekhans, T. S. Furey, R. A. Harte, F. Hsu, et al. 2006. The UCSC genome browser database: update 2006. *Nucleic Acids Res.* 34: D590–D598.
40. Zambelli, F., G. Pesole, and G. Pavesi. 2009. Pscan: finding over-represented transcription factor binding site motifs in sequences from co-regulated or co-expressed genes. *Nucleic Acids Res.* 37 W247–W252.
41. Andersson, R., C. Gebhard, I. Miguel-Escalada, I. Hoof, J. Bornholdt, M. Boyd, Y. Chen, X. Zhao, C. Schmidl, T. Suzuki, et al. 2014. An atlas of active enhancers across human cell types and tissues. *Nature* 507: 455–461.
42. Forrest, A. R., H. Kawaji, M. Rehli, J. K. Baillie, M. J. de Hoon, V. Haberle, T. Lassmann, I. V. Kulakovskiy, M. Lizio, M. Itoh, et al; FANTOM Consortium and the RIKEN PMI and CLST (DGT). 2014. A promoter-level mammalian expression atlas. *Nature* 507: 462–470.
43. Jin, V. X., G. A. Singer, F. J. Agosto-Pérez, S. Liyanarachchi, and R. V. Davuluri. 2006. Genome-wide analysis of core promoter elements from conserved human and mouse orthologous pairs. *BMC Bioinformatics* 7: 114.
44. Badis, G., M. F. Berger, A. A. Philippakis, S. Talukder, A. R. Gehrke, S. A. Jaeger, E. T. Chan, G. Metzler, A. Vedenko, X. Chen, et al. 2009. Diversity and complexity in DNA recognition by transcription factors. *Science* 324: 1720–1723.
45. Malhotra, D., E. Portales-Casamar, A. Singh, S. Srivastava, D. Arenillas, C. Happel, C. Shyr, N. Wakabayashi, T. W. Kensler, W. W. Wasserman, and S. Biswal. 2010. Global mapping of binding sites for Nrf2 identifies novel targets in cell survival response through ChIP-Seq profiling and network analysis. *Nucleic Acids Res.* 38: 5718–5734.
46. Fujita, P. A., B. Rhead, A. S. Zweig, A. S. Hinrichs, D. Karolchik, M. S. Cline, M. Goldman, G. P. Barber, H. Clawson, A. Coelho, et al. 2011. The UCSC genome browser database: update 2011. *Nucleic Acids Res.* 39: D876–D882.
47. Wei, G. H., G. Badis, M. F. Berger, T. Kivioja, K. Palin, M. Enge, M. Bonke, A. Jolma, M. Varjosalo, A. R. Gehrke, et al. 2010. Genome-wide analysis of ETS-family DNA-binding in vitro and in vivo. *EMBO J.* 29: 2147–2160.
48. Jolma, A., Y. Yin, K. R. Nitta, K. Dave, A. Popov, M. Taipale, M. Enge, T. Kivioja, E. Morgunova, and J. Taipale. 2015. DNA-dependent formation of transcription factor pairs alters their binding specificity. *Nature* 527: 384–388.
49. Najafabadi, H. S., S. Mnaimneh, F. W. Schmitges, M. Garton, K. N. Lam, A. Yang, M. Albu, M. T. Weirauch, E. Radovani, P. M. Kim, et al. 2015. C2H2 zinc finger proteins greatly expand the human regulatory lexicon. *Nat. Biotechnol.* 33: 555–562.
50. McLean, C. Y., D. Bristor, M. Hiller, S. L. Clarke, B. T. Schaar, C. B. Lowe, A. M. Wenger, and G. Bejerano. 2010. GREAT improves functional interpretation of *cis*-regulatory regions. *Nat. Biotechnol.* 28: 495–501.
51. Anders, S., P. T. Pyl, and W. Huber. 2015. HTSeq—a Python framework to work with high-throughput sequencing data. *Bioinformatics* 31: 166–169.
52. Curina, A., A. Termanini, I. Barozzi, E. Prosperini, M. Simonatto, S. Polletti, A. Silvola, M. Soldi, L. Austenaa, T. Bonaldi, et al. 2017. High constitutive activity of a broad panel of housekeeping and tissue-specific *cis*-regulatory elements depends on a subset of ETS proteins. *Genes Dev.* 31: 399–412.
53. Tong, A. J., X. Liu, B. J. Thomas, M. M. Lissner, M. R. Baker, M. D. Senagolage, A. L. Allred, G. D. Barish, and S. T. Smale. 2016. A stringent systems approach uncovers gene-specific mechanisms regulating inflammation. *Cell* 165: 165–179.
54. Robinson, J. T., H. Thorvaldsdóttir, W. Winckler, M. Guttman, E. S. Lander, G. Getz, and J. P. Mesirov. 2011. Integrative genomics viewer. *Nat. Biotechnol.* 29: 24–26.
55. Thorvaldsdóttir, H., J. T. Robinson, and J. P. Mesirov. 2013. Integrative genomics viewer (IGV): high-performance genomics data visualization and exploration. *Brief. Bioinform.* 14: 178–192.
56. Grant, C. E., T. L. Bailey, and W. S. Noble. 2011. FIMO: scanning for occurrences of a given motif. *Bioinformatics* 27: 1017–1018.
57. Bailey, T. L., M. Boden, F. A. Buske, M. Frith, C. E. Grant, L. Clementi, J. Ren, W. W. Li, and W. S. Noble. 2009. MEME SUITE: tools for motif discovery and searching. *Nucleic Acids Res.* 37: W202–W208.
58. Shevchenko, A., H. Tomas, J. Havlis, J. V. Olsen, and M. Mann. 2006. In-gel digestion for mass spectrometric characterization of proteins and proteomes. *Nat. Protoc.* 1: 2856–2860.
59. Rappsilber, J., M. Mann, and Y. Ishihama. 2007. Protocol for micro-purification, enrichment, pre-fractionation and storage of peptides for proteomics using StageTips. *Nat. Protoc.* 2: 1896–1906.
60. Cox, J., N. Neuhauser, A. Michalski, R. A. Scheltema, J. V. Olsen, and M. Mann. 2011. Andromeda: a peptide search engine integrated into the MaxQuant environment. *J. Proteome Res.* 10: 1794–1805.
61. Tyanova, S., T. Temu, P. Sinitcyn, A. Carlson, M. Y. Hein, T. Geiger, M. Mann, and J. Cox. 2016. The Perseus computational platform for comprehensive analysis of (prote)omics data. *Nat. Methods* 13: 731–740.
62. Cox, J., and M. Mann. 2008. MaxQuant enables high peptide identification rates, individualized p.p.b.-range mass accuracies and proteome-wide protein quantification. *Nat. Biotechnol.* 26: 1367–1372.
63. Takeyama, K., R. C. Aguiar, L. Gu, C. He, G. J. Freeman, J. L. Kutok, J. C. Aster, and M. A. Shipp. 2003. The BAL-binding protein BBAP and related Deltex family members exhibit ubiquitin-protein isopeptide ligase activity. *J. Biol. Chem.* 278: 21930–21937.
64. Ponpuak, M., A. S. Davis, E. A. Roberts, M. A. Delgado, C. Dinkins, Z. Zhao, H. W. Virgin, IV, G. B. Kyei, T. Johansen, I. Vergne, and V. Deretic. 2010. Delivery of cytosolic components by autophagic adaptor protein p62 endows autophagosomes with unique antimicrobial properties. *Immunity* 32: 329–341.
65. Komatsu, M., S. Kageyama, and Y. Ichimura. 2012. p62/SQSTM1/A170: physiology and pathology. *Pharmacol. Res.* 66: 457–462.
66. Moscat, J., M. Karin, and M. T. Diaz-Meco. 2016. p62 in cancer: signaling adaptor beyond autophagy. *Cell* 167: 606–609.
67. Bange, F. C., U. Vogel, T. Flohr, M. Kiekenbeck, B. Denecke, and E. C. Böttger. 1994. IFP 35 is an interferon-induced leucine zipper protein that undergoes interferon-regulated cellular redistribution. *J. Biol. Chem.* 269: 1091–1098.
68. Lebrun, S. J., R. L. Shpall, and L. Naumovski. 1998. Interferon-induced upregulation and cytoplasmic localization of Myc-interacting protein Nmi. *J. Interferon Cytokine Res.* 18: 767–771.
69. Zhou, X., J. Liao, A. Meyerdierks, L. Feng, L. Naumovski, E. C. Bottger, and M. B. Omary. 2000. Interferon-alpha induces nmi-IFP35 heterodimeric complex formation that is affected by the phosphorylation of IFP35. *J. Biol. Chem.* 275: 21364–21371.
70. Chen, J., R. L. Shpall, A. Meyerdierks, M. Hagemeier, E. C. Böttger, and L. Naumovski. 2000. Interferon-inducible Myc/STAT-interacting protein Nmi associates with IFP 35 into a high molecular mass complex and inhibits proteasome-mediated degradation of IFP 35. *J. Biol. Chem.* 275: 36278–36284.
71. Zhu, M., S. John, M. Berg, and W. J. Leonard. 1999. Functional association of Nmi with Stat5 and Stat1 in IL-2- and IFNγ-mediated signaling. *Cell* 96: 121–130.
72. Wang, X., L. M. Johansen, H. J. Tae, and E. J. Taparowsky. 1996. IFP 35 forms complexes with B-ATF, a member of the AP1 family of transcription factors. *Biochem. Biophys. Res. Commun.* 229: 316–322.
73. Doyle, S., S. Vaidya, R. O'Connell, H. Dadgostar, P. Dempsey, T. Wu, G. Rao, R. Sun, M. Haberland, R. Modlin, and G. Cheng. 2002. IRF3 mediates a TLR3/TLR4-specific antiviral gene program. *Immunity* 17: 251–263.
74. Creyghton, M. P., A. W. Cheng, G. G. Welstead, T. Kooistra, B. W. Carey, E. J. Steine, J. Hanna, M. A. Lodato, G. M. Frampton, P. A. Sharp, et al. 2010.

Histone H3K27ac separates active from poised enhancers and predicts developmental state. *Proc. Natl. Acad. Sci. USA* 107: 21931–21936.
75. Rada-Iglesias, A., R. Bajpai, T. Swigut, S. A. Brugmann, R. A. Flynn, and J. Wysocka. 2011. A unique chromatin signature uncovers early developmental enhancers in humans. *Nature* 470: 279–283.
76. Wyant, T. L., M. K. Tanner, and M. B. Sztein. 1999. *Salmonella typhi* flagella are potent inducers of proinflammatory cytokine secretion by human monocytes. *Infect. Immun.* 67: 3619–3624.
77. Rosenberger, C. M., M. G. Scott, M. R. Gold, R. E. Hancock, and B. B. Finlay. 2000. *Salmonella typhimurium* infection and lipopolysaccharide stimulation induce similar changes in macrophage gene expression. *J. Immunol.* 164: 5894–5904.
78. McPherson, R. L., R. Abraham, E. Sreekumar, S. E. Ong, S. J. Cheng, V. K. Baxter, H. A. Kistemaker, D. V. Filippov, D. E. Griffin, and A. K. Leung. 2017. ADP-ribosylhydrolase activity of Chikungunya virus macrodomain is critical for virus replication and virulence. *Proc. Natl. Acad. Sci. USA* 114: 1666–1671.
79. Iwata, H., C. Goettsch, A. Sharma, P. Ricchiuto, W. W. Goh, A. Halu, I. Yamada, H. Yoshida, T. Hara, M. Wei, et al. 2016. PARP9 and PARP14 cross-regulate macrophage activation via STAT1 ADP-ribosylation. *Nat. Commun.* 7: 12849.
80. Jiang, M., and M. J. Imperiale. 2012. Design stars: how small DNA viruses remodel the host nucleus. *Future Virol.* 7: 445–459.
81. Whittaker, G. R., M. Kann, and A. Helenius. 2000. Viral entry into the nucleus. *Annu. Rev. Cell Dev. Biol.* 16: 627–651.